

Supplementary Materials for
**Control of the overpotential of a [FeFe] hydrogenase mimic by a
synthetic second coordination sphere**

Sandra S. Nurttila,^[a] Riccardo Zaffaroni,^[a] Simon Mathew,^[a] and Joost N. H. Reek^{*[a]}

[a] Dr. S. S. Nurttila, Dr. R. Zaffaroni, Dr. S. Mathew, Prof. Dr. J. N. H. Reek

Homogeneous, Supramolecular and Bio-Inspired Catalysis, Van 't Hoff Institute for Molecular
Sciences

University of Amsterdam

Science Park 904, 1098XH Amsterdam (The Netherlands)

Email: j.n.h.reek@uva.nl

Contents

1. Materials and methods.....	3
2. Synthesis and characterization of cage building block Zn-L	4
3. Synthesis and characterization of Fe₄(Zn-L)₆	6
4. xTB calculations	12
5. Characterization of 1·Fe₄(Zn-L)₆	15
6. UV-vis binding study between 1 and Fe₄(Zn-L)₆	19
7. General titration fitting procedure.....	21
8. Electro- and spectroelectrochemistry of 1 and 1·Fe₄(Zn-L)₆	23
9. ¹ H NMR study of 1 in the presence of HNEt ₃ PF ₆	28
10. UV-vis study of 1·Fe₄(Zn-L)₆ in the presence of HNEt ₃ PF ₆	28
11. References	29

1. Materials and methods

All reactions were carried out under an atmosphere of N₂ using standard Schlenk techniques unless otherwise noted. All solvents were distilled prior to use by conventional methods. Complex **1** was prepared according to a literature procedure.¹ The supporting electrolyte *n*Bu₄NPF₆ was prepared from saturated solution of KPF₆ and *n*Bu₄NBr in water and recrystallized from hot methanol and dried under vacuum at 80 °C overnight. The acid HNEt₃PF₆ was prepared following a literature procedure.² All other reagents were purchased from commercial suppliers and used without further purification.

NMR spectroscopy

¹H NMR spectra were recorded on a Bruker AV300 and AV400 spectrometer and they are referenced to the solvent residual signal (5.32 ppm for CD₂Cl₂, 7.32 ppm for CDCl₃, 1.32 ppm for CD₃CN and 8.03 ppm for DMF-d₇). 2D ¹H DOSY spectral data were acquired with temperature and magnetic gradient calibration prior to the measurements, and the temperature was kept at 298 K during the measurements.

Mass spectrometry

High resolution mass spectra were collected on a HR-ToF Bruker Daltonik GmbH (Bremen, Germany) Impact II, an ESI-ToF MS capable of resolution of at least 40000 FWHM, which was coupled to a Bruker cryospray unit. Detection was in positive-ion mode and the source voltage was between 4 and 6 kV. The flow rates were 18 uL/hr. The drying gas (N₂) was held at -35 °C and the spray gas was held at -40 °C. The machine was calibrated prior to every experiment via direct infusion of a TFA-Na solution, which provided a *m/z* range of singly charged peaks up to 3500 Da in both ion modes.

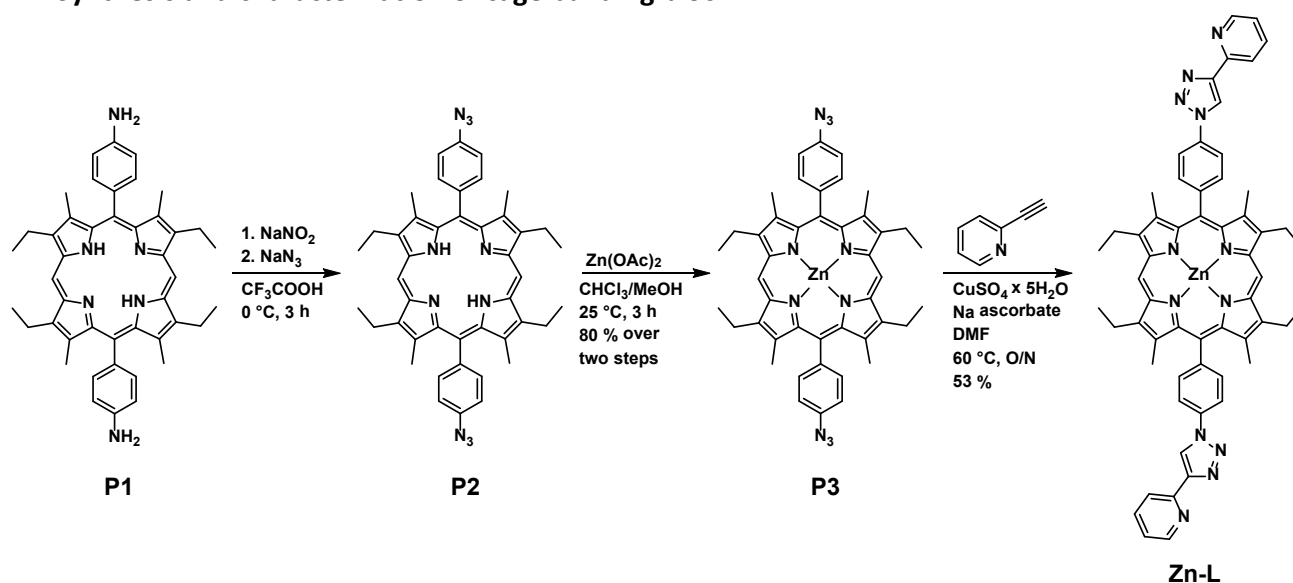
Steady state UV-vis spectroscopy

Steady state UV-Vis spectra were acquired on a single beam Hewlett Packard 8453 spectrometer in a quartz cuvette with a path length of 10 mm using the solvent as a background. For the determination of the binding constant, a solution of Fe₄(Zn-L)₆ kept at a constant concentration of 5.5 μM was titrated with an increasing concentration of **1**. The obtained titration curves were then fitted to a 1:2 host-guest model using a Matlab script.³

Electrochemistry

Cyclic voltammetry was acquired of deaerated solutions in freshly distilled acetonitrile. The voltammograms were recorded in a gas-tight single compartment 3-electrode cell with a glassy carbon working electrode, a platinum wire as auxiliary electrode and a leakless Ag/AgCl (3 M KCl) reference electrode (Metrohm 6.0750.100). A 663-VA stand was used along with a PGSTAT302N potentiostat (Metrohm/Autolab). All redox potentials are reported against the ferrocene/ferrocenium (Fc/Fc⁺) redox couple used as internal standard. In electrocatalytic studies different amounts of the acid HNEt₃PF₆ dissolved in acetonitrile were added with a microsyringe into the solution in the CV cell.

2. Synthesis and characterization of cage building block Zn-L



P1 was synthesized using a literature procedure⁴ and **Zn-L** was synthesized using a modified literature procedure⁵:

P2:

P1 (0.29 g, 0.43 mmol) was dissolved in CF_3COOH (5 mL) to give a dark green solution that was cooled to 0°C . A solution of NaNO_2 (0.12 g, 1.74 mmol) in deionized water (1.3 mL) was added dropwise, and after stirring for 10 min a solution of NaN_3 (0.23 g, 3.47 mmol) in deionized water (1.3 mL) was added dropwise over a period of 10 min. The solution was stirred at 0°C for 2 h, where after it was carefully quenched by the addition of aqueous Na_2CO_3 solution until all effervescence stopped. The purple suspension was extracted with ethyl acetate (3x 50 mL) and from the combined organic layers the solvent was removed under vacuum to give **P2** as a purple solid. The product was used as such without further purification. ^1H NMR (300 MHz, CDCl_3) δ (ppm) = 10.24 (s, 2H), 8.05 (d, $J = 8.3$ Hz, 4H), 7.43 (d, $J = 8.3$ Hz, 4H), 4.02 (q, $J = 7.7$ Hz, 8H), 2.53 (s, 12H), 1.77 (t, $J = 7.5$ Hz, 12H), -2.46 (s, 2H).

P3:

Crude **P2** (0.31 g, 0.43 mmol, assuming 100% yield) was dissolved in chloroform (93 mL) and a solution of $\text{Zn}(\text{OAc})_2 \times 2\text{H}_2\text{O}$ (0.48 g, 2.17 mmol) in methanol (6 mL) was added. The purple solution was stirred at room temperature covered from light for 4 h and the reaction progress was monitored by TLC. When the reaction had completed, the solvent was removed under vacuum to give a purple solid. The crude product was purified by column chromatography (silica, eluent: dichloromethane) to give **P3** as a purple solid in 80% yield starting from **P1**. ^1H NMR (300 MHz, CD_2Cl_2) δ (ppm) = 10.22 (s, 2H), 8.06 (d, $J = 8.1$ Hz, 4H), 7.45 (d, $J = 8.2$ Hz, 4H), 4.03 (q, $J = 7.5$ Hz, 8H), 2.53 (s, 12H), 1.78 (t, $J = 7.5$ Hz, 12H).

Zn-L:

P3 (0.17 g, 0.21 mmol), sodium ascorbate (0.026 g, 0.13 mmol) and 2-ethynylpyridine (65 μL , 0.64 mmol) were dissolved in *N,N*-dimethylformamide (50 mL), and the resulting purple solution was sonicated for 20 min. $\text{CuSO}_4 \times 5\text{H}_2\text{O}$ (0.043 g, 0.17 mmol) was added as a solid and the solution was again sonicated for 20 min. The solution was stirred at 60°C for 20 h, followed by cooling to room temperature. The solution was diluted with deionized water and extracted with dichloromethane (4x 100 mL), and finally the combined organic layers were washed with deionized water. The solvent was removed under vacuum to give a purple solid. The crude product was purified by column chromatography (silica, eluent:

tetrahydrofuran/hexane = 1:1) to give **Zn-L** as a purple solid in 53% yield. ^1H NMR (500 MHz, DMF-d_7) δ (ppm) = 10.27 (s, 2H), 9.71 (s, 2H), 8.82 – 8.77 (d, J = 7.9 Hz, 2H), 8.62 (d, J = 7.9 Hz, 4H), 8.46 – 8.40 (d, J = 10.0 Hz, 4H), 8.34 (d, J = 7.8 Hz, 2H), 8.12 – 8.04 (m, 2H), 7.50 (dd, J = 7.7, 4.8 Hz, 2H), 4.09 (q, J = 5.0 Hz, 8H), 2.61 (s, 12H), 1.79 (t, J = 7.5 Hz, 12H). HRMS (ESI+) calc. for $[\text{Zn-L}]^+$ ($\text{C}_{58}\text{H}_{52}\text{N}_{12}\text{Zn}_1^+$) 981.38076, found 981.3812.

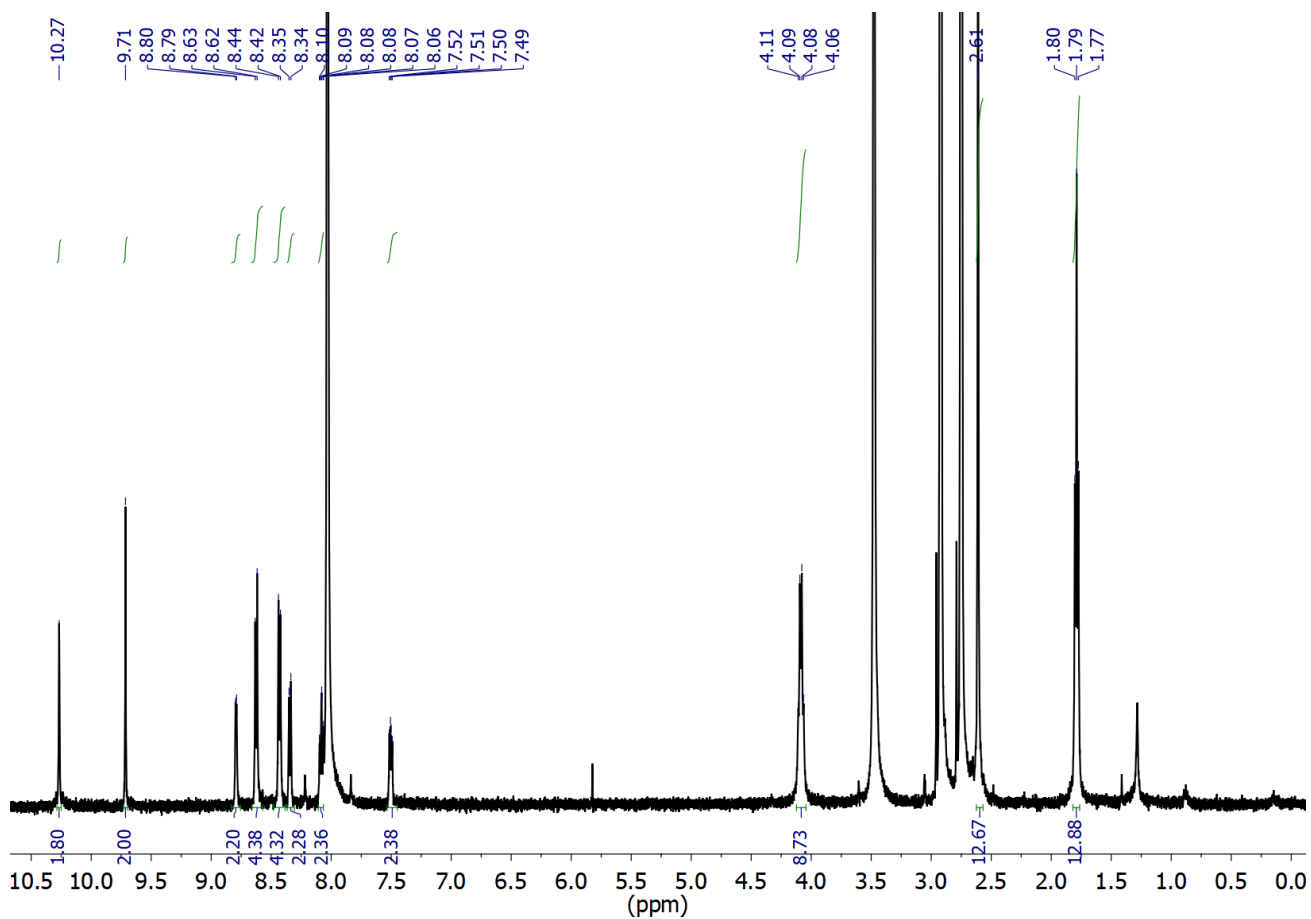
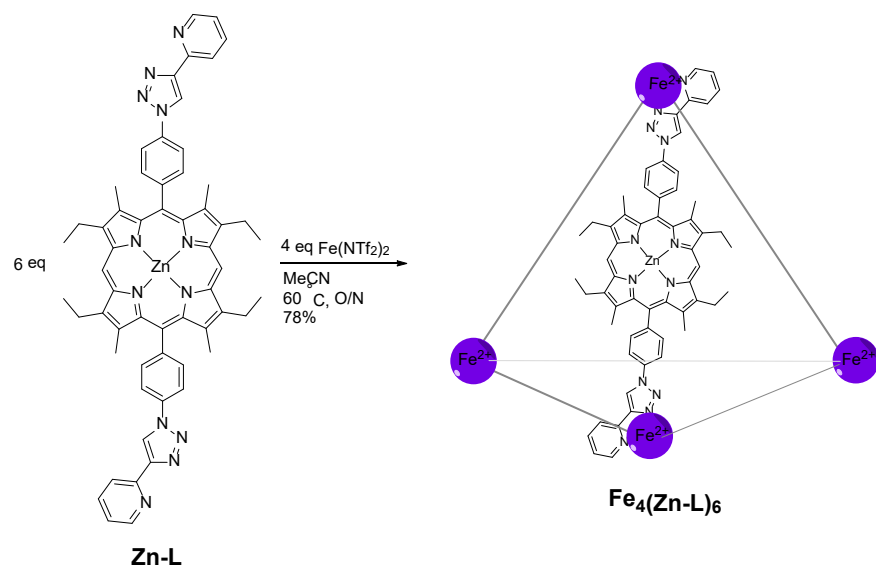


Figure S 1. ^1H NMR (500 MHz, 298 K) spectrum of **Zn-L** in DMF-d_7 .

3. Synthesis and characterization of $\text{Fe}_4(\text{Zn-L})_6$



Zn-L (8.2 mg, 8.3 μmol) and $\text{Fe}(\text{NTf}_2)_2$ (3.4 mg, 5.6 μmol) were transferred along with degassed and dry acetonitrile (2 mL) into a Schlenk flask under N_2 . The purple suspension was heated at 70°C overnight. Subsequently, the resulting dark purple solution was cooled down to room temperature and added dropwise into diethyl ether (10 mL) to give rise to a purple suspension. The solid was recovered by vacuum filtration, where after it was further washed with diethyl ether (2 x 4 mL). The residual diethyl ether was removed to give pure $\text{Fe}_4(\text{Zn-L})_6$ as a purple, microcrystalline solid in 78% yield. ^1H NMR (500 MHz, $\text{MeCN-}d_3$) δ (ppm) = 10.28 (d, J = 33.6 Hz, 2H), 9.82 – 9.70 (m, 2H), 8.52 (d, J = 9.8 Hz, 2H), 8.45 – 8.24 (m, 10H), 8.09 (m, 2H), 7.69 (m, 2H), 4.12 (d, J = 47.3 Hz, 8H), 2.71 – 2.44 (m, 12H), 1.80 (m, 12H). DOSY NMR (CD_3CN , 298 K): $\log D$ = -9.0. HRMS (ESI+) calc. (found) = 764.7469 (764.7433) [$\text{Fe}_4(\text{Zn-L})_6(\text{NTf}_2)_0$] $^{8+}$, 913.9847 (913.9782) [$\text{Fe}_4(\text{Zn-L})_6(\text{NTf}_2)_1$] $^{7+}$, 1112.9684 (1112.9588) [$\text{Fe}_4(\text{Zn-L})_6(\text{NTf}_2)_2$] $^{6+}$, 1391.7456 (1391.7346) [$\text{Fe}_4(\text{Zn-L})_6(\text{NTf}_2)_3$] $^{5+}$, 1809.6614 (1809.6468) [$\text{Fe}_4(\text{Zn-L})_6(\text{NTf}_2)_4$] $^{4+}$.

Crystallization attempts:

1. Slow vapour diffusion of diethyl ether into an acetonitrile solution of the cage (several concentrations attempted) at room temperature and 4°C.
2. Slow vapour diffusion of ethyl acetate into N,N-dimethylformamide solution of the cage (several concentrations attempted) at room temperature and 4°C.

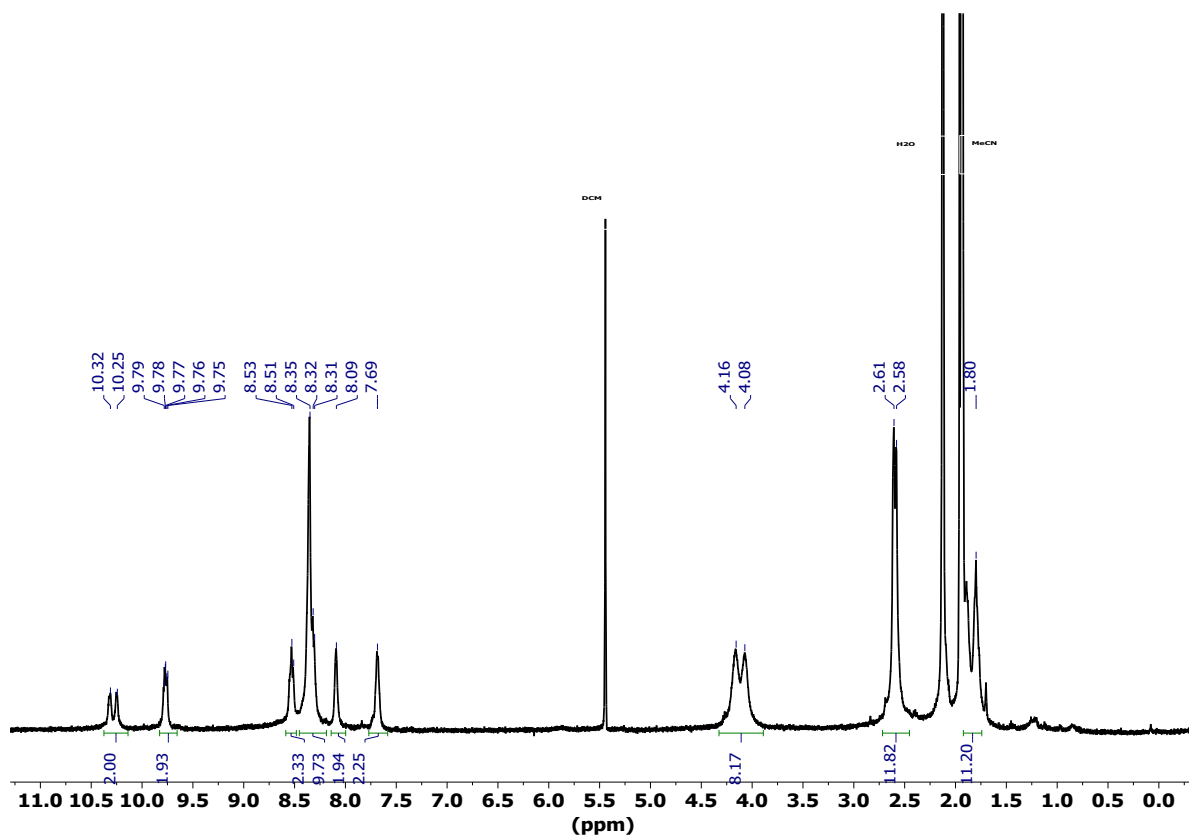


Figure S 2. ^1H NMR (300 MHz, 298 K) spectrum of $\text{Fe}_4(\text{Zn-L})_6$ in CD_3CN .

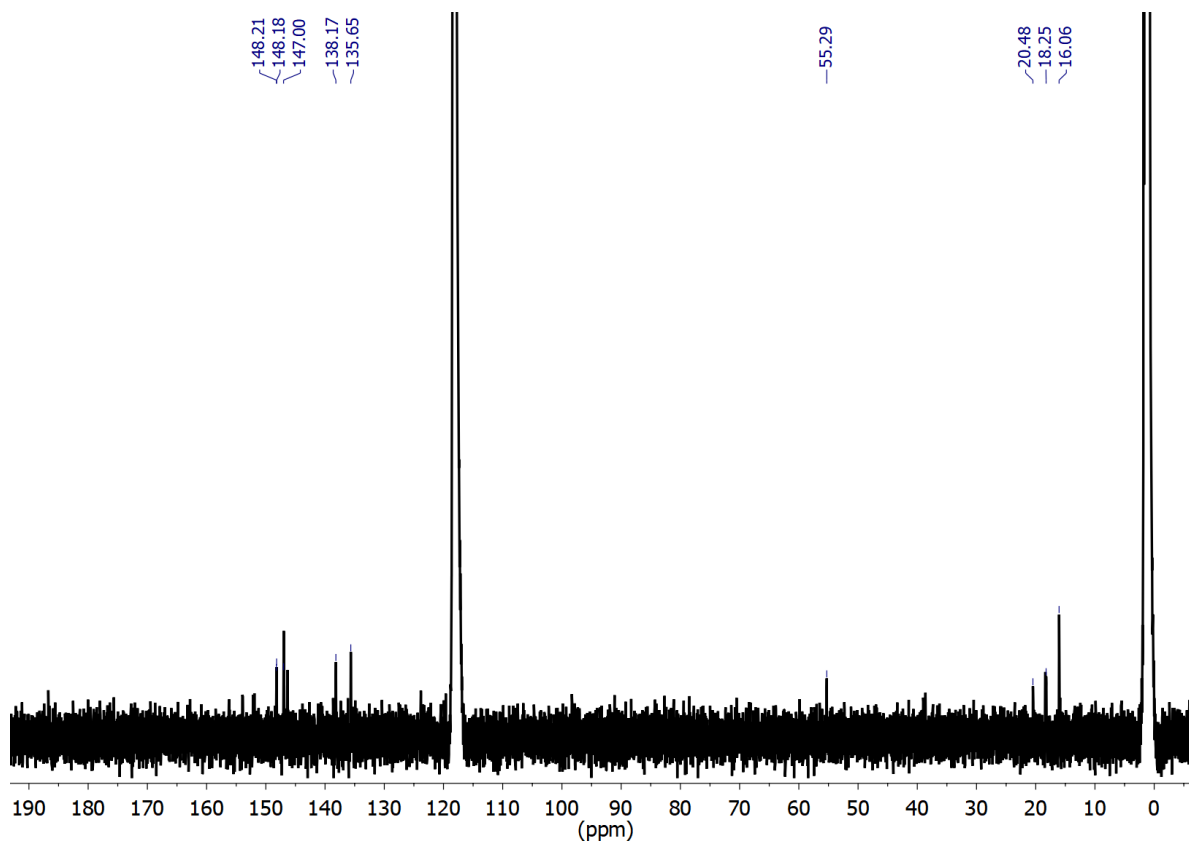


Figure S 3. ^{13}C NMR (75 MHz, 298 K) spectrum $\text{Fe}_4(\text{Zn-L})_6$ in CD_3CN .

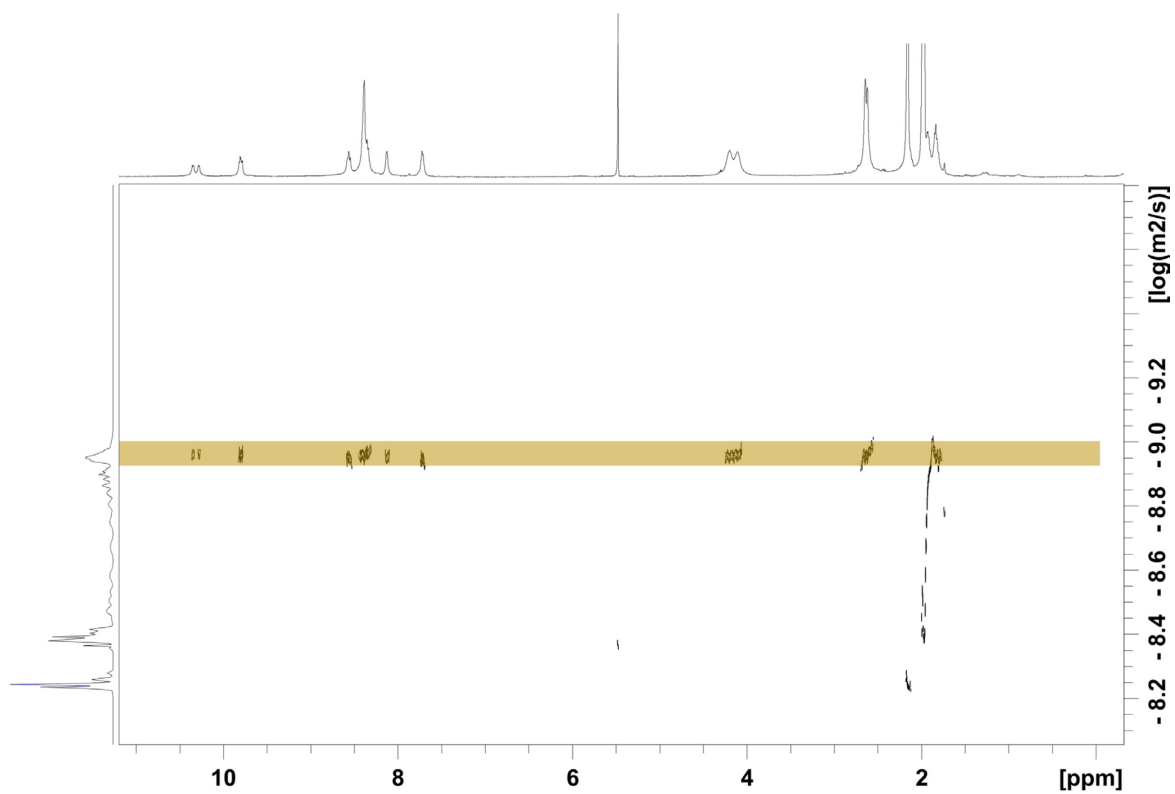


Figure S 4. 2D ^1H DOSY (500 MHz, 298 K) spectrum of $\text{Fe}_4(\text{Zn-L})_6$ in CD_3CN . The diffusion coefficient of $\text{Fe}_4(\text{Zn-L})_6$ was measured to be $1.0 \times 10^{-9} \text{ m}^2 \text{ s}^{-1}$, corresponding to a hydrodynamic radius of around 1.3 nm.

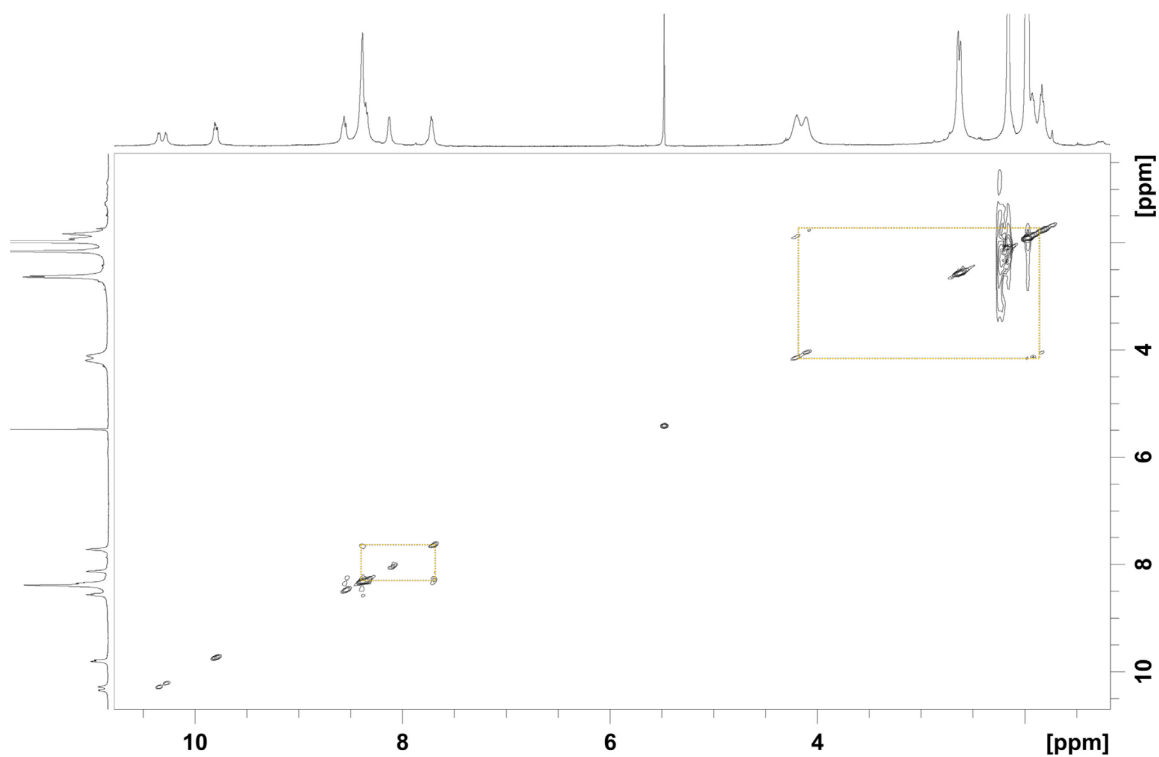


Figure S 5. 2D ^1H - ^1H COSY (500 MHz, 298 K) spectrum of $\text{Fe}_4(\text{Zn-L})_6$ in CD_3CN .

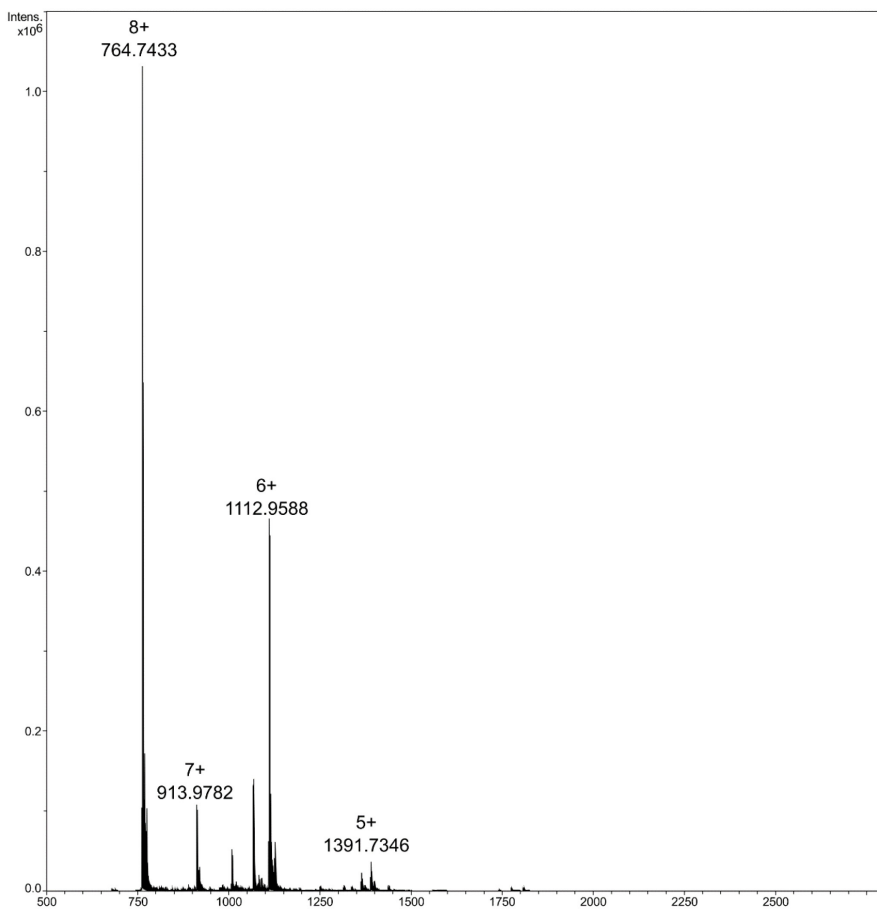


Figure S 6. CSI mass spectrum (full spectrum) of $\text{Fe}_4(\text{Zn-L})_6$ with a spray temperature of $-40\text{ }^\circ\text{C}$ and a dry gas temperature of $-35\text{ }^\circ\text{C}$.

Table S 1. Different charged species observed in the CSI mass spectrum of $\text{Fe}_4(\text{Zn-L})_6$ and the corresponding found and calculated $[m/z]$.

Species	Charge	Found $[m/z]$	Calculated $[m/z]$
$\text{Fe}_4(\text{Zn-L})_6(\text{NTf}_2)_0$	8+	764.7433	764.7469
$\text{Fe}_4(\text{Zn-L})_6(\text{NTf}_2)_1$	7+	913.9782	913.9847
$\text{Fe}_4(\text{Zn-L})_6(\text{NTf}_2)_2$	6+	1112.9588	1112.9684
$\text{Fe}_4(\text{Zn-L})_6(\text{NTf}_2)_3$	5+	1391.7346	1391.7456
$\text{Fe}_4(\text{Zn-L})_6(\text{NTf}_2)_4$	4+	1809.6468	1809.6614

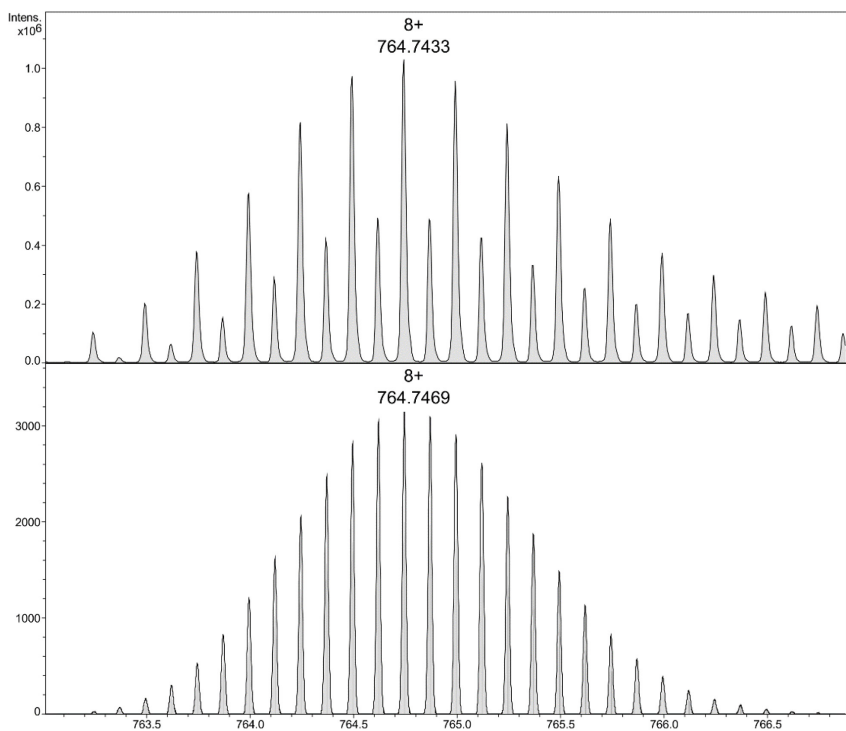


Figure S 7. Expanded spectrum for the charged species $[\text{Fe}_4(\text{Zn-L})_6(\text{NTf}_2)_0]^{8+}$ observed (above) in the CSI mass spectrum of $\text{Fe}_4(\text{Zn-L})_6$ and simulated isotopic distribution (below). The difference in intensity between the peaks in the experimental spectrum is due to a symmetrical fragmentation of the cage.

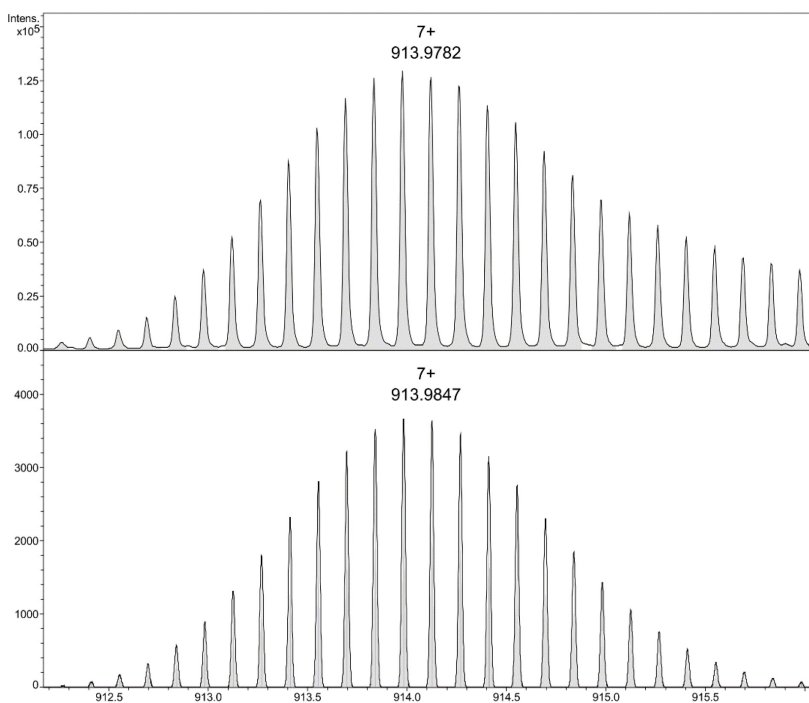


Figure S 8. Expanded spectrum for the charged species $[\text{Fe}_4(\text{Zn-L})_6(\text{NTf}_2)_1]^{7+}$ observed (above) in the CSI mass spectrum of $\text{Fe}_4(\text{Zn-L})_6$ and simulated isotopic distribution (below).

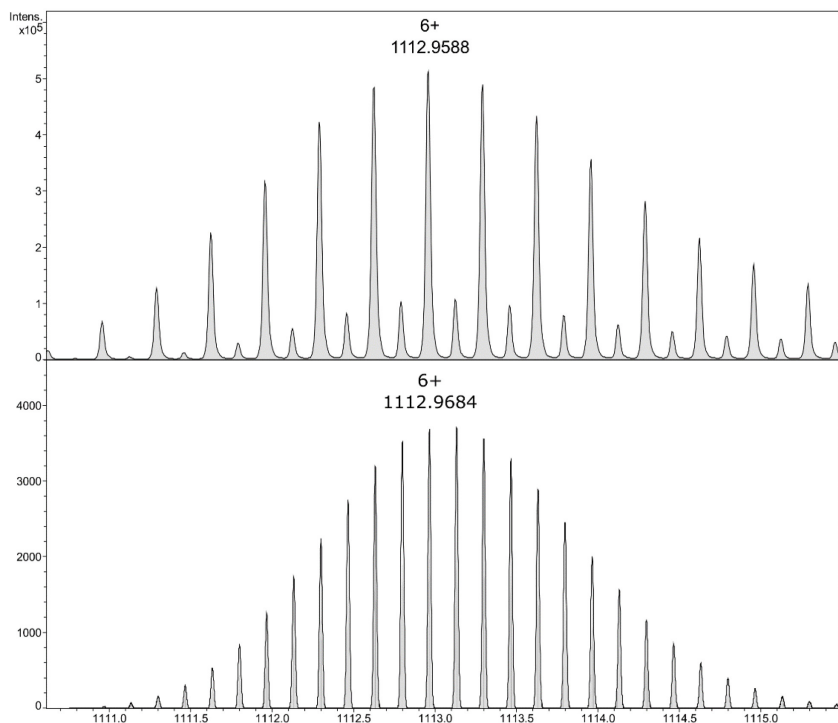


Figure S 9. Expanded spectrum for the charged species $[\text{Fe}_4(\text{Zn-L})_6(\text{NTf}_2)_2]^{6+}$ observed (above) in the CSI mass spectrum of $\text{Fe}_4(\text{Zn-L})_6$ and simulated isotopic distribution (below). The difference in intensity between the peaks in the experimental spectrum is due to a symmetrical fragmentation of the cage.

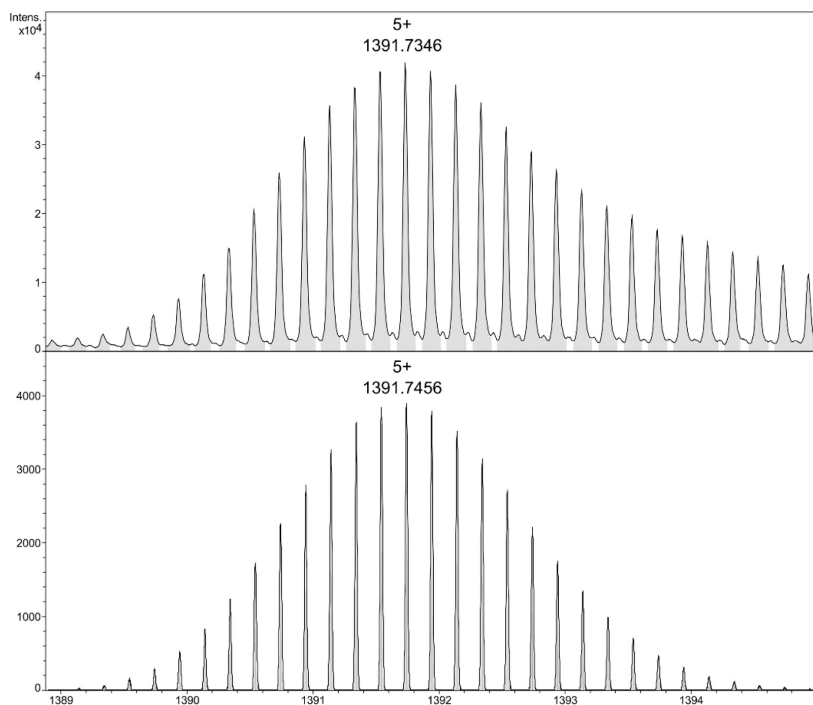


Figure S 10. Expanded spectrum for the charged species $[\text{Fe}_4(\text{Zn-L})_6(\text{NTf}_2)_3]^{5+}$ observed (above) in the CSI mass spectrum of $\text{Fe}_4(\text{Zn-L})_6$ and simulated isotopic distribution (below).

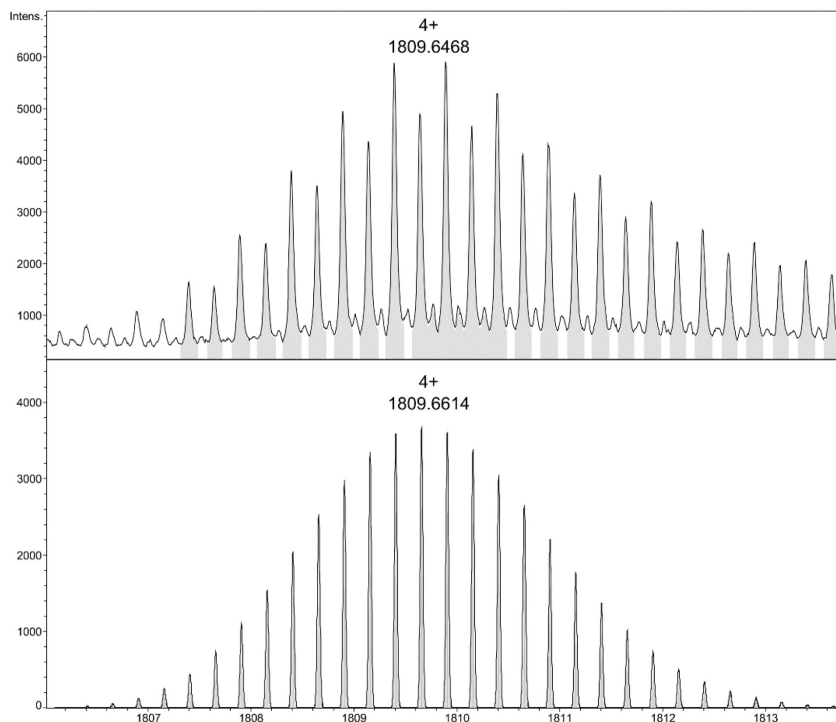


Figure S 11. Expanded spectrum for the charged species $[\text{Fe}_4(\text{Zn-L})_6(\text{NTf}_2)_4]^{4+}$ observed (above) in the CSI mass spectrum of $\text{Fe}_4(\text{Zn-L})_6$ and simulated isotopic distribution (below). The difference in intensity between the peaks in the experimental spectrum is due to a symmetrical fragmentation of the cage.

4. xTB calculations

Geometry optimizations of $\text{Fe}_4(\text{Zn-L})_6$ and $\mathbf{1} \cdot \text{Fe}_4(\text{Zn-L})_6$ were carried out with the program ADF using a tight-binding quantum chemical method (GFN-xTB) that mimics DFT and is useful for large molecular systems.⁶ The average $\text{N}_{\text{py}}\text{-N}_{\text{py}}$ distance in **1** is 6 Å, which is suitable for encapsulation in the cage in which the average Zn-Zn distance is 11 Å. A typical distance for a slightly bent $\text{N}_{\text{py}}\text{-Zn}$ coordination bond is 2.2 Å.⁷ A single Fe-Zn distance in the cage is around 15 Å, in line with the size obtained from DOSY NMR studies. The effective window aperture size of the cage is around 5 Å, indicating that the catalyst cannot freely diffuse in and out of the cage. From the calculations it can be concluded that a single Zn- N_{py} interaction between **1** and the inner cavity of cage $\text{Fe}_4(\text{Zn-L})_6$ is formed. This is likely due to the *meta* orientation of the pyridine groups, which is not optimal for binding inside the cage. Coordinates of the computed structures are given in a separate pdf file.

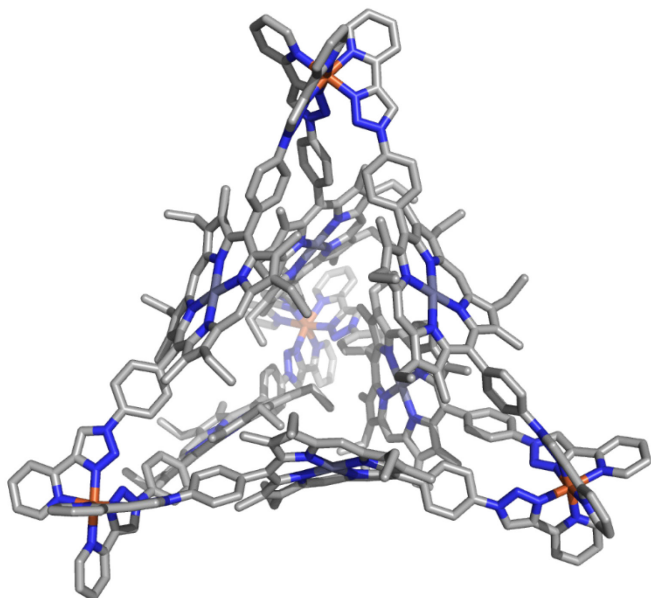


Figure S 12. xTB geometry optimized structure of $\text{Fe}_4(\text{Zn-L})_6$ in stick model.

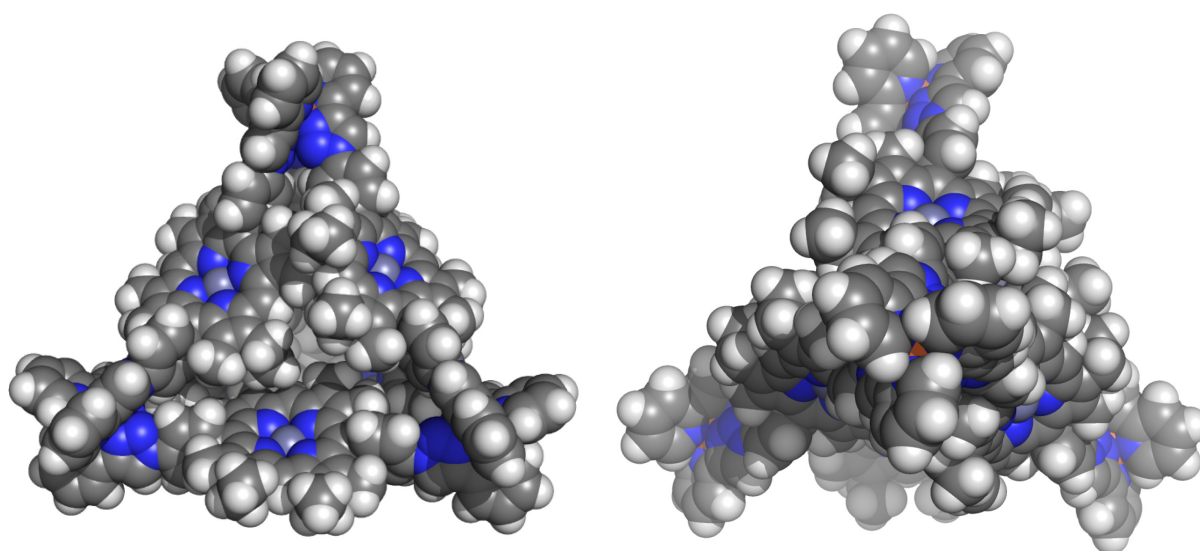


Figure S 13. xTB geometry optimized structure of $\text{Fe}_4(\text{Zn-L})_6$ in space-filling model. (left) Side view. (right) Top view.

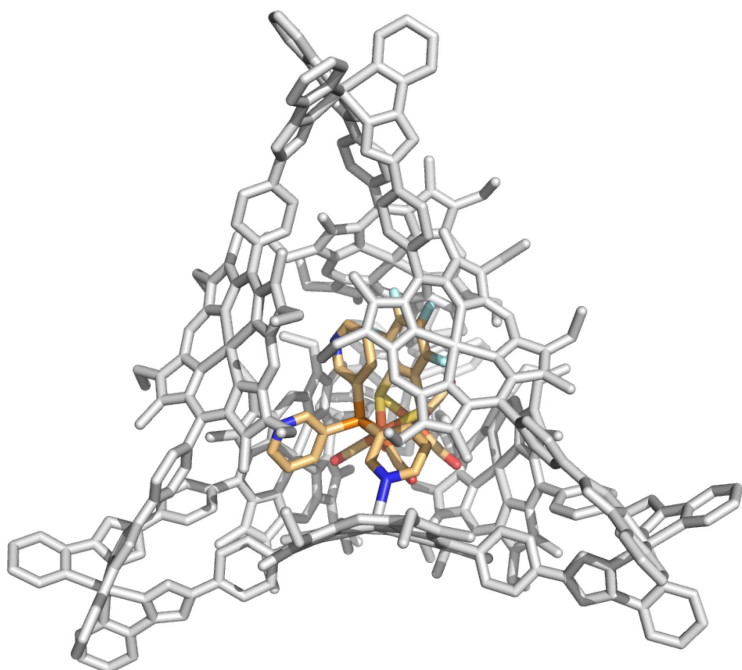


Figure S 14. xTB geometry optimized structure of $1 \cdot \text{Fe}_4(\text{Zn-L})_6$ in stick model showing one $\text{N}_{\text{py}}\text{-Zn}$ coordination bond between **1** and $\text{Fe}_4(\text{Zn-L})_6$.

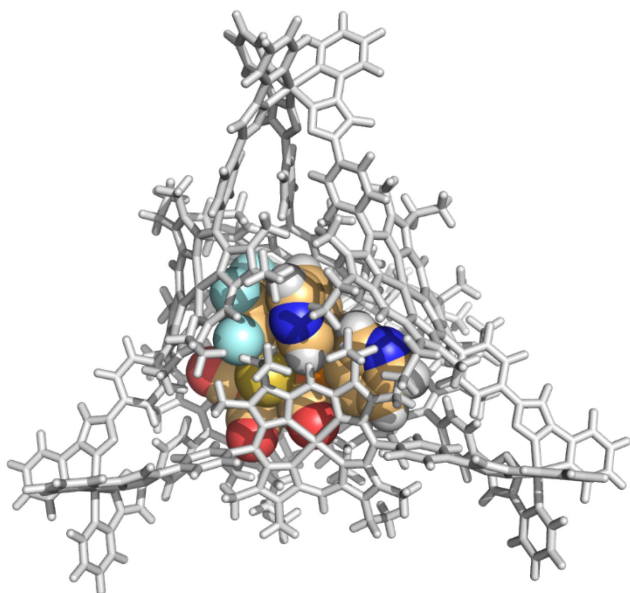


Figure S 15. xTB geometry optimized structure of $1 \cdot \text{Fe}_4(\text{Zn-L})_6$ in space-filling model showing one $\text{N}_{\text{py}}\text{-Zn}$ coordination bond between **1** and $\text{Fe}_4(\text{Zn-L})_6$.

5. Characterization of $1 \cdot \text{Fe}_4(\text{Zn-L})_6$

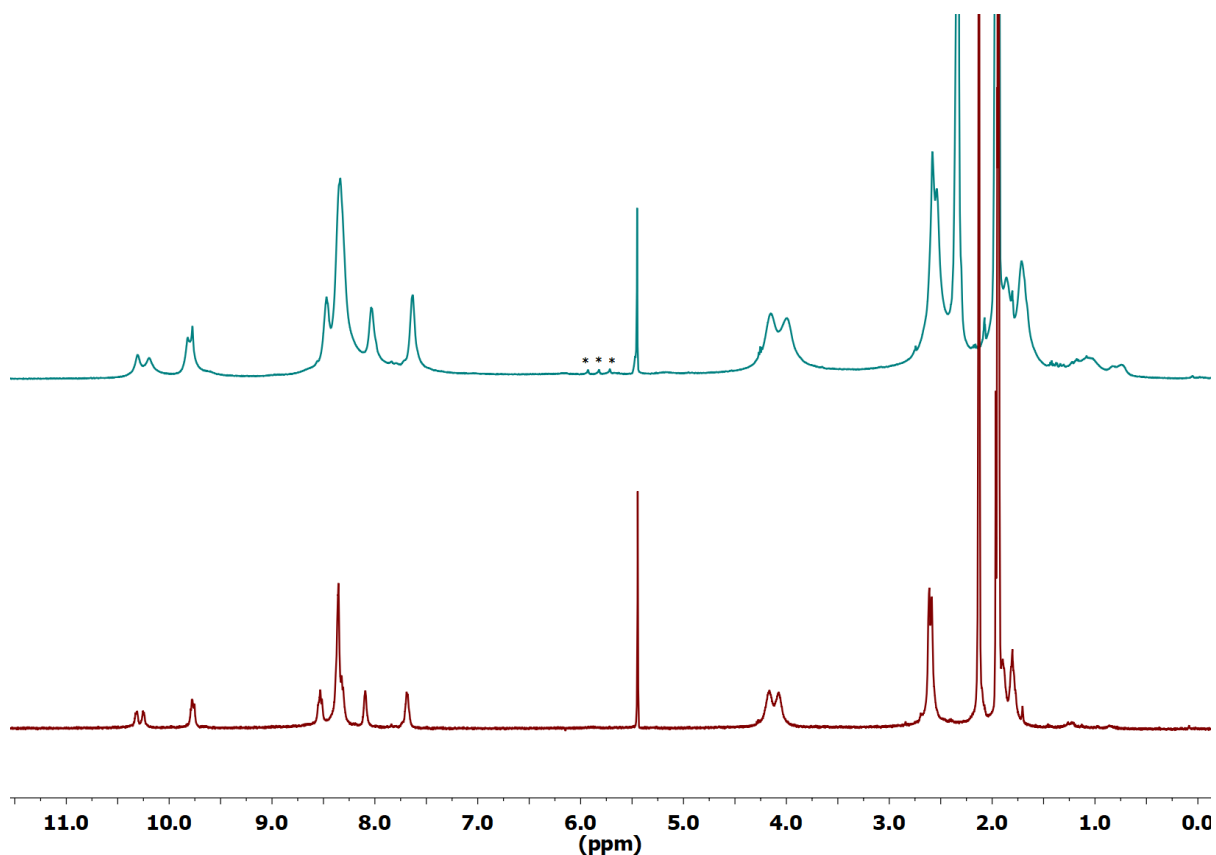


Figure S 16. ^1H NMR (500 MHz, CD_3CN) spectrum of (top) $1 \cdot \text{Fe}_4(\text{Zn-L})_6$ at 233 K and (bottom) $\text{Fe}_4(\text{Zn-L})_6$ at 298 K. The peaks belonging to the encapsulated **1** have been marked with stars in the top spectrum.

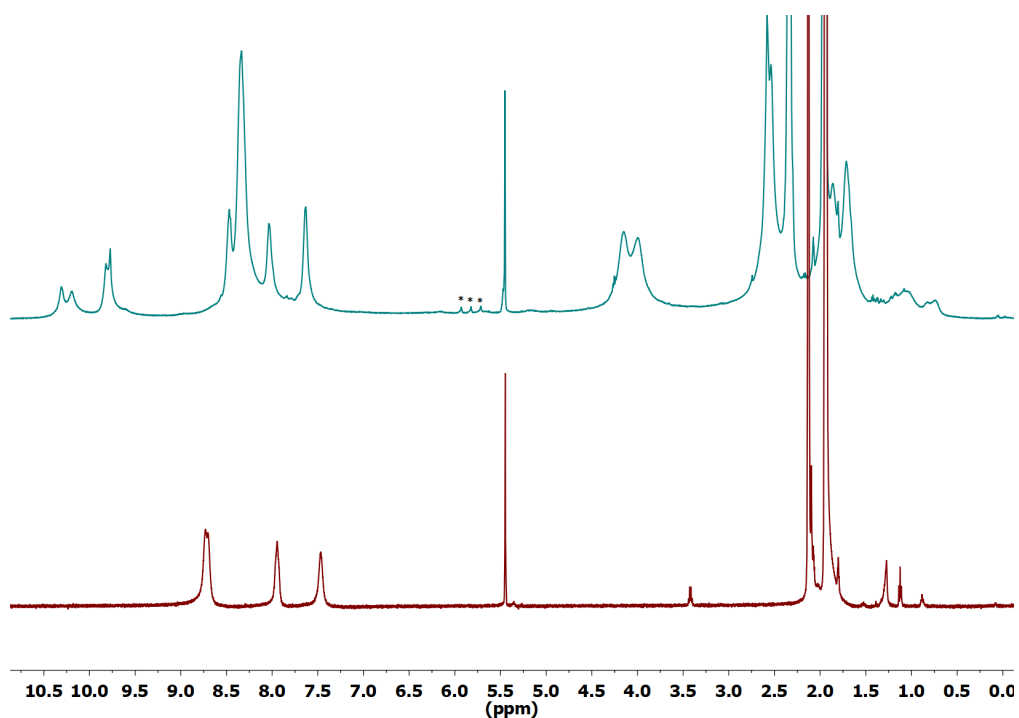


Figure S 17. ^1H NMR (500 MHz, CD_3CN , 298 K) spectrum of (top) $1 \cdot \text{Fe}_4(\text{Zn-L})_6$ and (bottom) **1**. The peaks belonging to the encapsulated **1** have been marked with stars in the top spectrum.

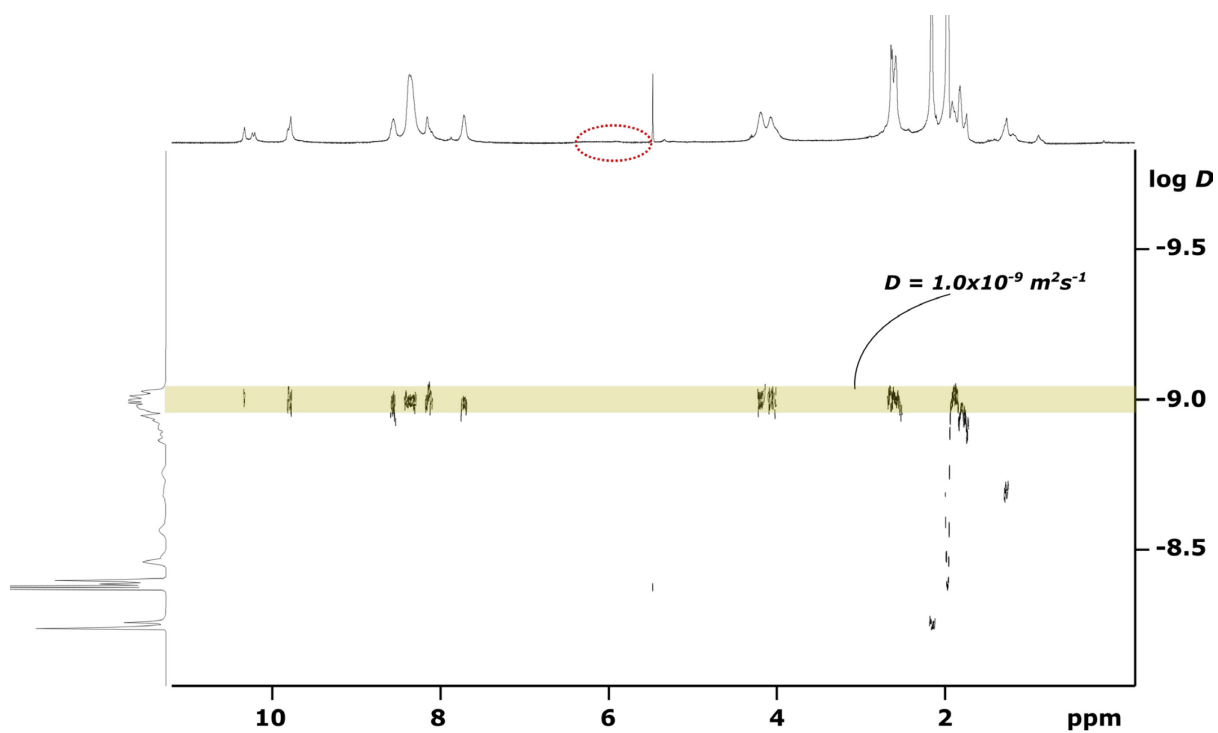


Figure S 18. 2D ^1H DOSY (500 MHz, 298 K) spectrum of $\mathbf{1} \cdot \text{Fe}_4(\text{Zn-L})_6$ in CD_3CN . The diffusion coefficient of $\mathbf{1} \cdot \text{Fe}_4(\text{Zn-L})_6$ was measured to be $1.0 \times 10^{-9} \text{ m}^2 \text{ s}^{-1}$, corresponding to a hydrodynamic radius of around 1.3 nm.

In the mass spectrum of **1**·Fe₄(Zn-L)₆ charge states 8+ and 5+ are visible, corresponding to different numbers of [(CF₃SO₂)₂N]⁻ counter-ions lost during ionization in the spectrometer. For each charge state the experimental and simulated isotope pattern match perfectly, confirming the elemental composition of the host-guest complex. Quantitative encapsulation of **1** inside the cage is not observed due to the low concentration applied in the mass experiment, as evident from signals with m/z ratios of 729 and 764 arising from free catalyst and empty cage. Additionally, other signals are observed in the mass spectrum that cannot be assigned to any specific species, and they are likely to arise from reactions of the un-encapsulated catalyst and cage inside the mass spectrometer.

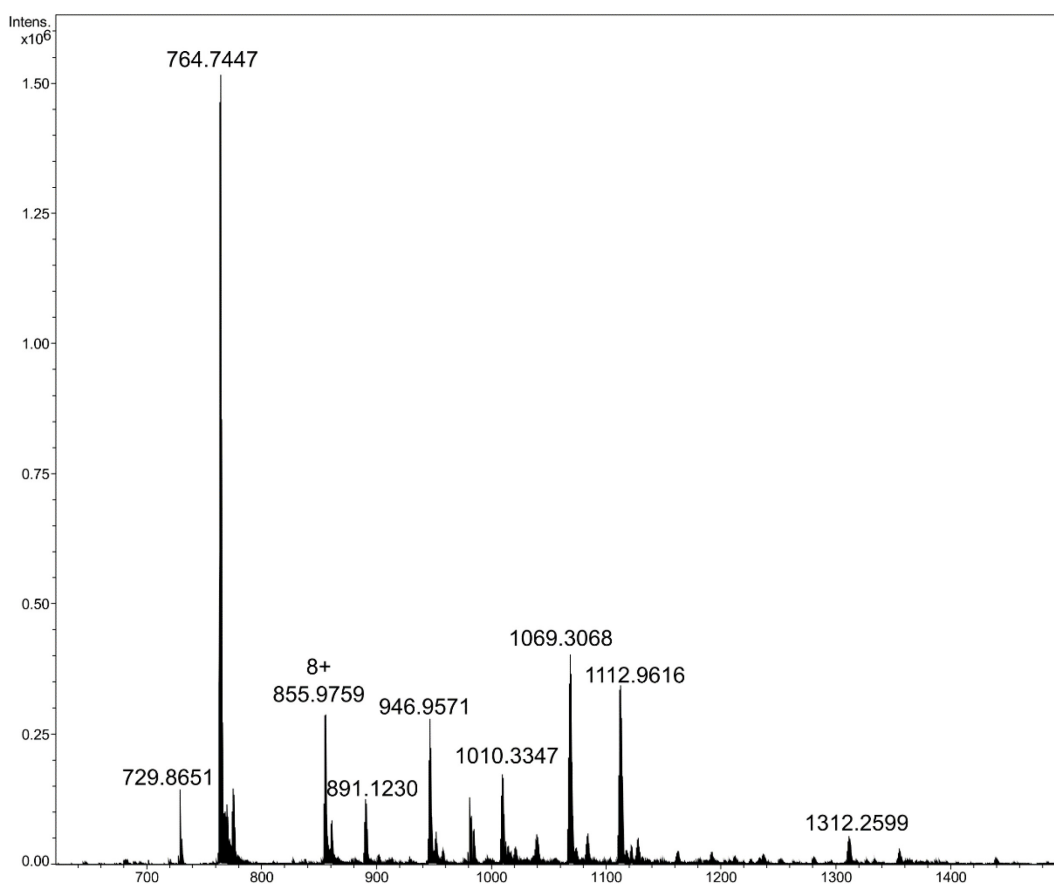


Figure S 19. CSI mass spectrum (full spectrum) of **1**·Fe₄(Zn-L)₆ with a spray temperature of -40 °C and a dry gas temperature of -35 °C. Signal with m/z ratio of 729.8651 corresponds to free **1** and signal with m/z ratio of 764.7447 corresponds to empty Fe₄(Zn-L)₆.

Table S 2. Different charged species observed in the CSI mass spectrum of **1**·Fe₄(Zn-L)₆ and the corresponding found and calculated [m/z].

Species	Charge	Found [m/z]	Calculated [m/z]
Fe ₄ (Zn-L) ₆ (1) ₁ (NTf ₂) ₀	8+	855.8508	855.8544
Fe ₄ (Zn-L) ₆ (1) ₁ (NTf ₂) ₃	5+	1537.5085	1537.5176

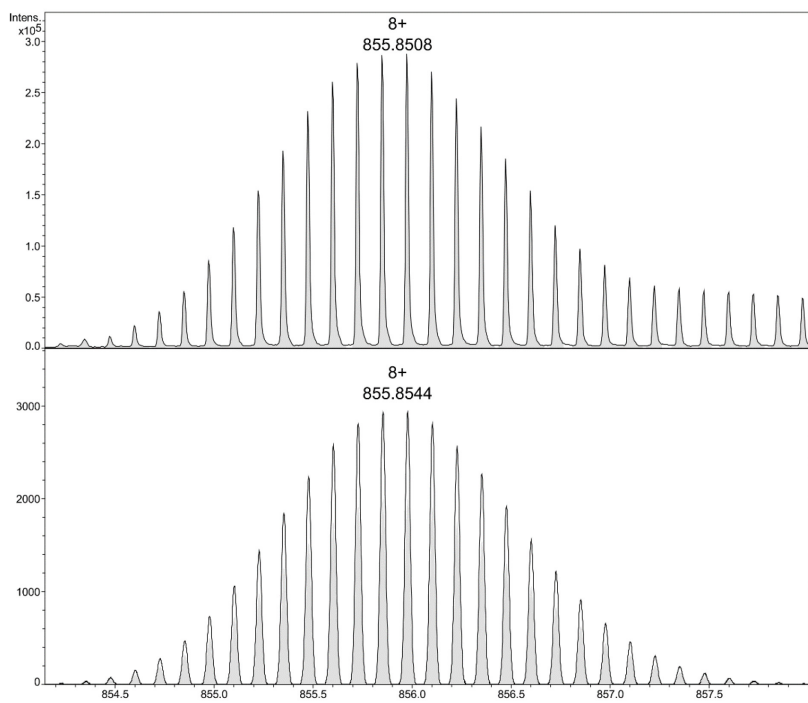


Figure S 20. Expanded spectrum for the charged species $[\text{Fe}_4(\text{Zn-L})_6(1)_1(\text{NTf}_2)_0]^{8+}$ observed (above) in the CSI mass spectrum of $1 \cdot \text{Fe}_4(\text{Zn-L})_6$ and simulated isotopic distribution (below).

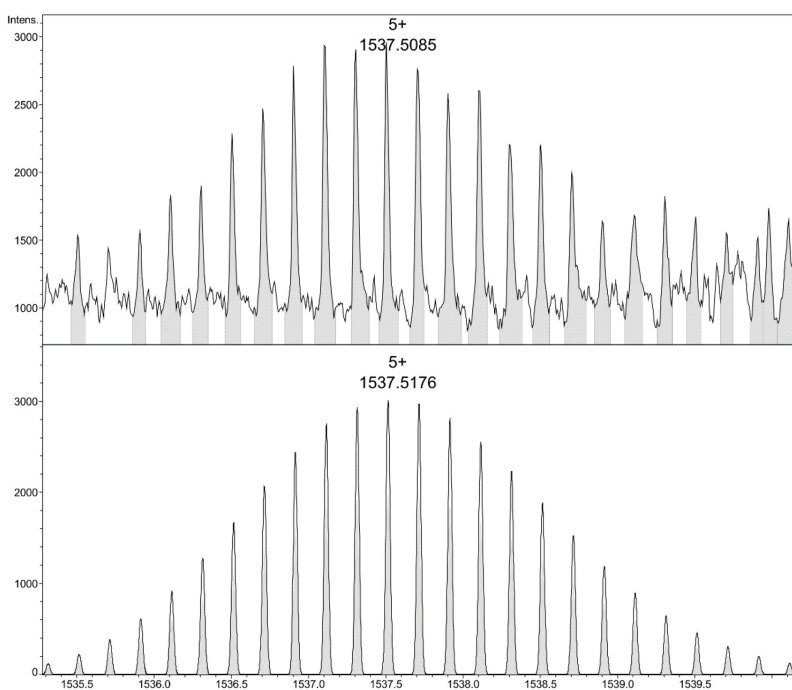


Figure S 21. Expanded spectrum for the charged species $[\text{Fe}_4(\text{Zn-L})_6(1)_1(\text{NTf}_2)_3]^{5+}$ observed (above) in the CSI mass spectrum of $1 \cdot \text{Fe}_4(\text{Zn-L})_6$ and simulated isotopic distribution (below).

6. UV-vis binding study between **1** and $\text{Fe}_4(\text{Zn-L})_6$

Complex **1** bears three pyridine groups with the nitrogen atoms in the *meta*-position, but based on molecular modelling studies a single Zn–N_{py} interaction is expected upon encapsulation of **1**. During the titration, the cage $\text{Fe}_4(\text{Zn-L})_6$ concentration is kept constant, adding increasing amounts of guest **1** in acetonitrile at 298 K. The bathochromic shift of the Soret and Q bands of the cage porphyrins are consistent with axial pyridine coordination (Figure 5).⁸ After the addition of around 30 equivalents of guest, all three isosbestic points at the Q bands are lost. This is consistent with the occurrence of two sequential binding events; strong binding followed by weaker binding.⁹ This indicates strong binding of one complex inside the cage, and a weaker monotopic binding at the outside of the cage at higher guest concentration, in line with molecular modelling that showed that only a single complex fits inside the cavity. Indeed, the best fit with the least error is obtained with a 1:2 host–guest equilibrium model, yielding microscopic binding constants $K_1 = 1.3 \cdot 10^4 \text{ M}^{-1}$ and $K_2 = 1.6 \cdot 10^3 \text{ M}^{-1}$. The binding constants suggest that indeed binding is via a single pyridine, as ditopic binding should lead to higher binding constants. Importantly, the binding is sufficiently high to ensure virtually quantitative binding of complex **1** when working at mM concentrations.

Table S 3. Fitting results for the 1:2 host-guest system between $\text{Fe}_4(\text{Zn-L})_6$ and **1** in acetonitrile for $K = 1.3 \times 10^4 \text{ M}^{-1}$ at 298 K, where $\alpha_1 = 0.12$.

Wavelength [nm]	$\epsilon_{\text{HG}} / 10^4$	$\epsilon_{\text{HGG}} / 10^5$	R^2
555	6.33	1.23	0.993
578	2.56	0.34	0.973
583	2.61	0.56	0.908

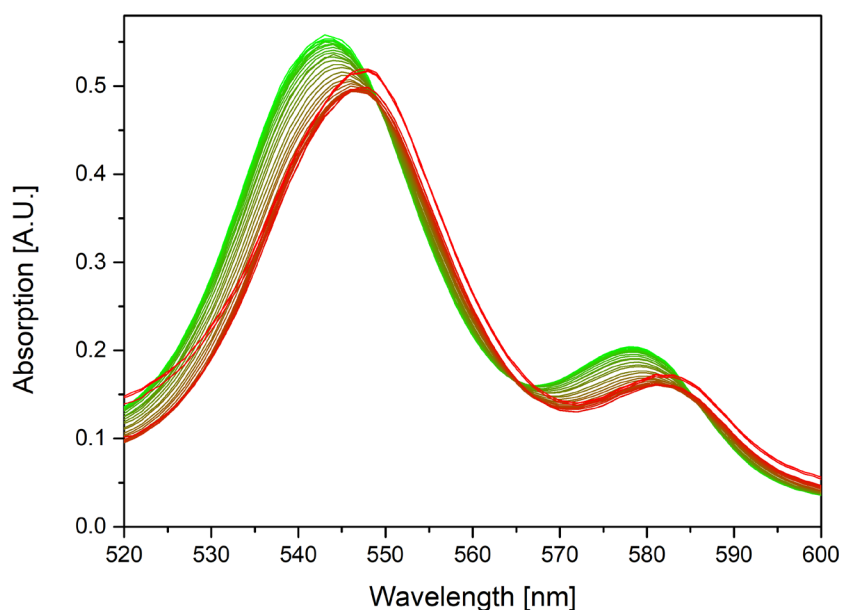


Figure S 22. Overlay of UV-vis spectra of the titration of $\text{Fe}_4(\text{Zn-L})_6$ (host) with **1** (guest), at a fixed host concentration of 5.5 μM in acetonitrile at 298 K.

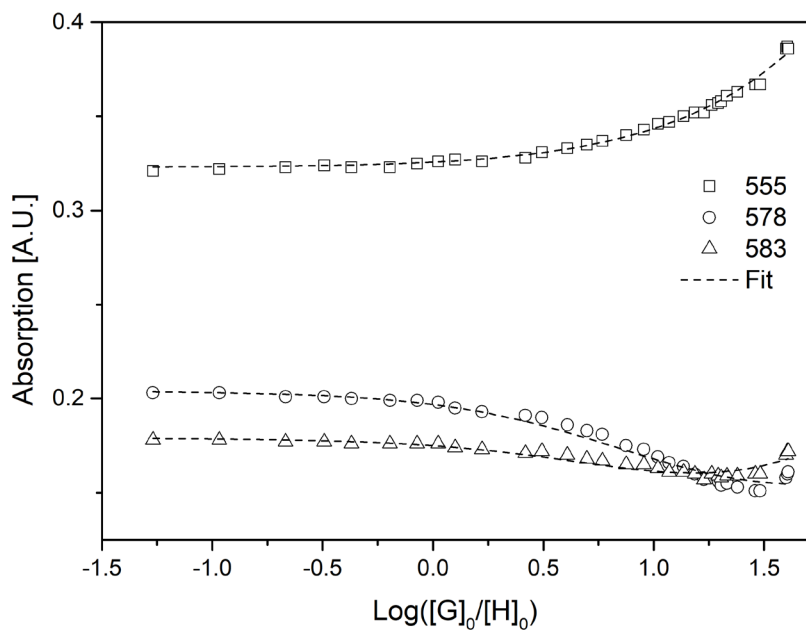


Figure S 23. Fitted UV-vis titration curves of $\text{Fe}_4(\text{Zn-L})_6$ with **1** in acetonitrile (298 K).

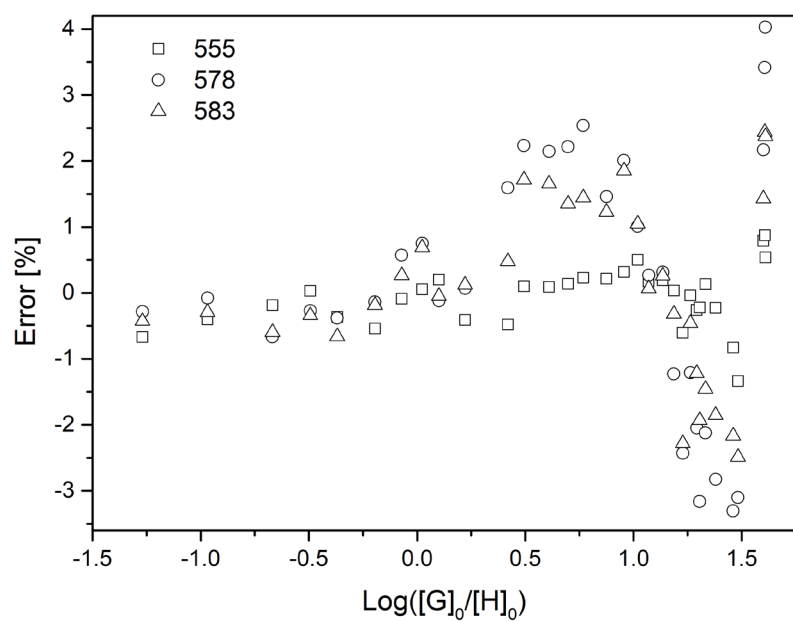


Figure S 24. Error distribution for the fitted curves of $\text{Fe}_4(\text{Zn-L})_6$ with **1** in acetonitrile (298 K).

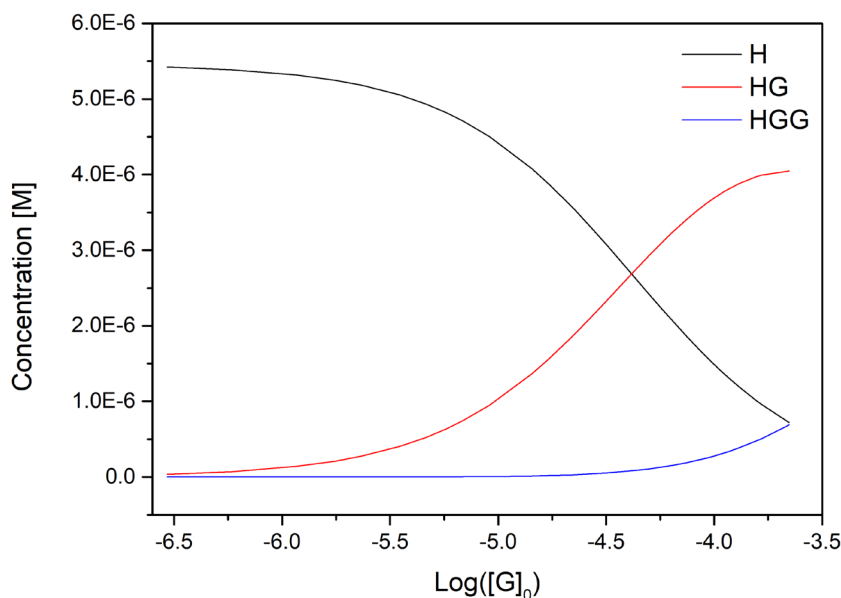


Figure S 25. Calculated species concentration of the titration of **Fe₄(Zn-L)₆** with **1** in acetonitrile (298 K).

7. General titration fitting procedure

Regardless of the supramolecular model and spectroscopic method, the fitting procedure for the determination of the association constants is as follows: At each titration point n in N (the total number of titration points) the initial concentrations for the host and guest species $[H]_{0,n}$ and $[G]_{0,n}$ are known, as are the observed values for either chemical shift $\delta_{\text{atom,obs},n}$ or absorption $A_{\lambda,\text{obs},n}$, which we will collectively call $O_{\text{obs},n}$. The fitting procedure is based around the COBYLA numerical optimization routine¹⁰ which tries to minimise the difference between the observed values and calculated values, given the constraint that association constants and concentrations are greater than zero:

$$\begin{aligned} \text{minimize} \quad & F_n = |O_{\text{obs},n} - O_{\text{calc},n}|, \quad n \in N \\ \text{subject to} \quad & \{[S]_n; K; \alpha\} \geq 0 \quad n \in N, \text{ for all species } S = \{H, G, HG, HGG, \dots\} \end{aligned}$$

The objective function F_n for the optimisation procedure calculates $O_{\text{calc},n}$ through the formulae for A_λ or δ_{atom} (*vide supra*). E.g. in the case of a 1:1 HG titration followed by UV-vis, the objective function becomes:

$$F_n = |O_{\text{obs},n} - O_{\text{calc},n}| = |A_{\text{obs},n} - A_{\text{calc},n}| = |A_{\text{obs},n} - \epsilon_H[H] + \epsilon_{HG}[HG]|$$

Given initial guesses for the association constants $\{K; \alpha\}$, $[H]$ and $[HG]$ can be calculated from the initial concentrations $[H]_0$ and $[G]_0$. Since the fitting procedure calls this routine very often (in our cases roughly between 10^2 and 10^6 times per fitting procedure, depending on the size of the problem (e.g. HG versus HGG)), we use a ‘rapid numerical integration algorithm for finding the equilibrium state of a system of coupled binding reactions’.¹¹ The objective function is then evaluated using initial guesses for the species coefficients (δ or ϵ), and the optimisation routine determines whether a minimum has been found or that the initial guesses have to be adjusted to provide a better fit to the data.

When a minimum has been found, the error distributions (difference between calculated and observed values) are visually checked for trends. If trends are observed that point towards a different model (e.g. cooperativity *versus* no cooperativity, or HGG *versus* HGGG), these models are fitted to the data as well and the different error distributions are compared between models.

Initial guesses and quality of fit

Since multi-parameter optimisations are difficult problems to accurately solve (many parameters, few observables), the quality of the fit should be scrutinised: The microscopic association constant in larger (e.g. 1:2) systems should be in the range for the same constant in the 1:1 system in the same solvent. The species coefficients (δ or ϵ) have to make sense, such that e.g. in the case of a HHHG system where the host H is tracked by UV-vis, the relation $\epsilon_{HG} \approx \frac{1}{2} \epsilon_{HHG} \approx \frac{1}{3} \epsilon_{HHHG}$ should hold, since the absorptivity per 'bound host' molecule shouldn't change appreciably in the system. Initial guesses for the optimisation procedure are made using similar, simplified relations and ideas, where e.g. in a HHHG UV-vis titration, almost all host molecules are bound in the HG form at the end of the titration curve, allowing for an estimate of ϵ_{HG} and thereby estimates of all other coefficients. Starting from these 'proper' guesses, the optimisation routine is generally both fastest *and* most accurate.

The accuracy of these optimisations turns out to be an ill-defined problem in supramolecular chemistry.¹² Our current understanding of this problem (after fitting a broad range of 'bad' and 'good' titrations), is that non-accurate additions during titrations translate *directly* into a noisy energy landscape with a noisy minimum. Combined with the fact that optimisation routines can never guarantee to find a global minimum, the found minimum is heavily dependent on the quality of the titration data and on the direction through which the minimum is approached (i.e. the initial guesses). Thus, when a minimum is found by the optimisation routine, we approach this minimum from multiple sides to assure this is in fact a global minimum, or to get an estimate on the size of the minimum. E.g. if we approach a one-dimensional problem from two extreme initial guesses and find minima at 900 and 1100, respectively, we conclude that the actual minimum is somewhere between these values and thereby immediately get a rough estimate of the accuracy with which we can determine the association constant.

The software used to fit the data is available here: limhes.net/optim

8. Electro- and spectroelectrochemistry of 1 and 1·Fe₄(Zn-L)₆

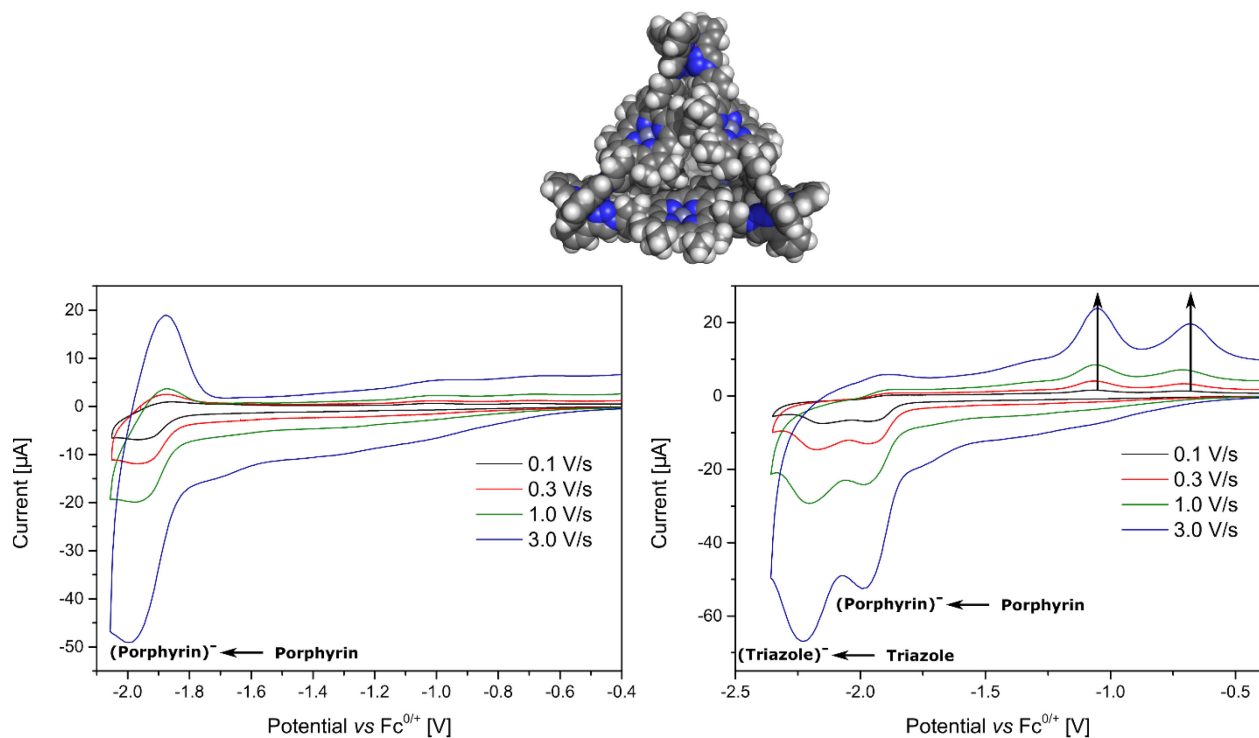


Figure S 26. Redox chemistry of Fe₄(Zn-L)₆ in the absence of acid. (left) Scan rate dependence of the cyclic voltammogram of 0.1 mM Fe₄(Zn-L)₆ in acetonitrile containing 0.1 M nBu₄NPF₆ as electrolyte. (right) Scan rate dependence of the cyclic voltammogram of 0.1 mM Fe₄(Zn-L)₆ in acetonitrile containing 0.1 M nBu₄NPF₆ as electrolyte in a larger potential window. The arrows indicate two waves that appear after the second reduction wave at -2.3 V (vs Fc/Fc⁺).

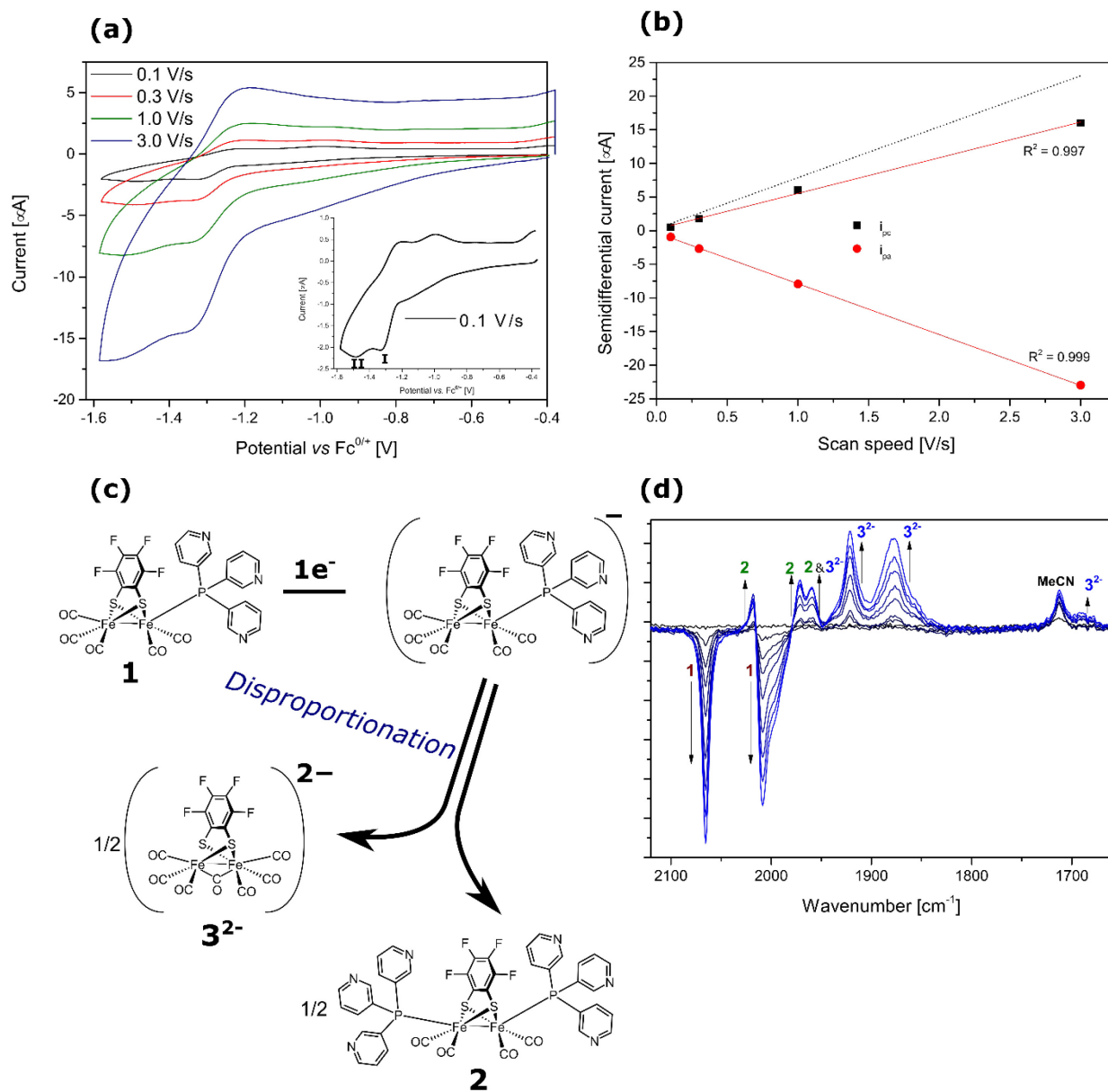


Figure S 27. Redox chemistry of **1** in the absence of acid. (a) Scan rate dependence of the cyclic voltammogram of 0.1 mM **1** in acetonitrile containing 0.1 M *n*Bu₄NPF₆ as electrolyte. The inset shows the voltammogram recorded at 0.1 V/s to depict the two redox waves I and II more clearly. (b) Plot of the semidifferential peak current of the reduction wave of **1** against the scan speed indicating that the redox event is solution-based but not reversible. The black dotted line would be observed for a fully reversible redox event. (c) Disproportionation of **1** upon reduction of the complex. (d) IR spectral evolution during the reduction of 1 mM **1** in acetonitrile containing 0.2 M *n*Bu₄NPF₆ as electrolyte.

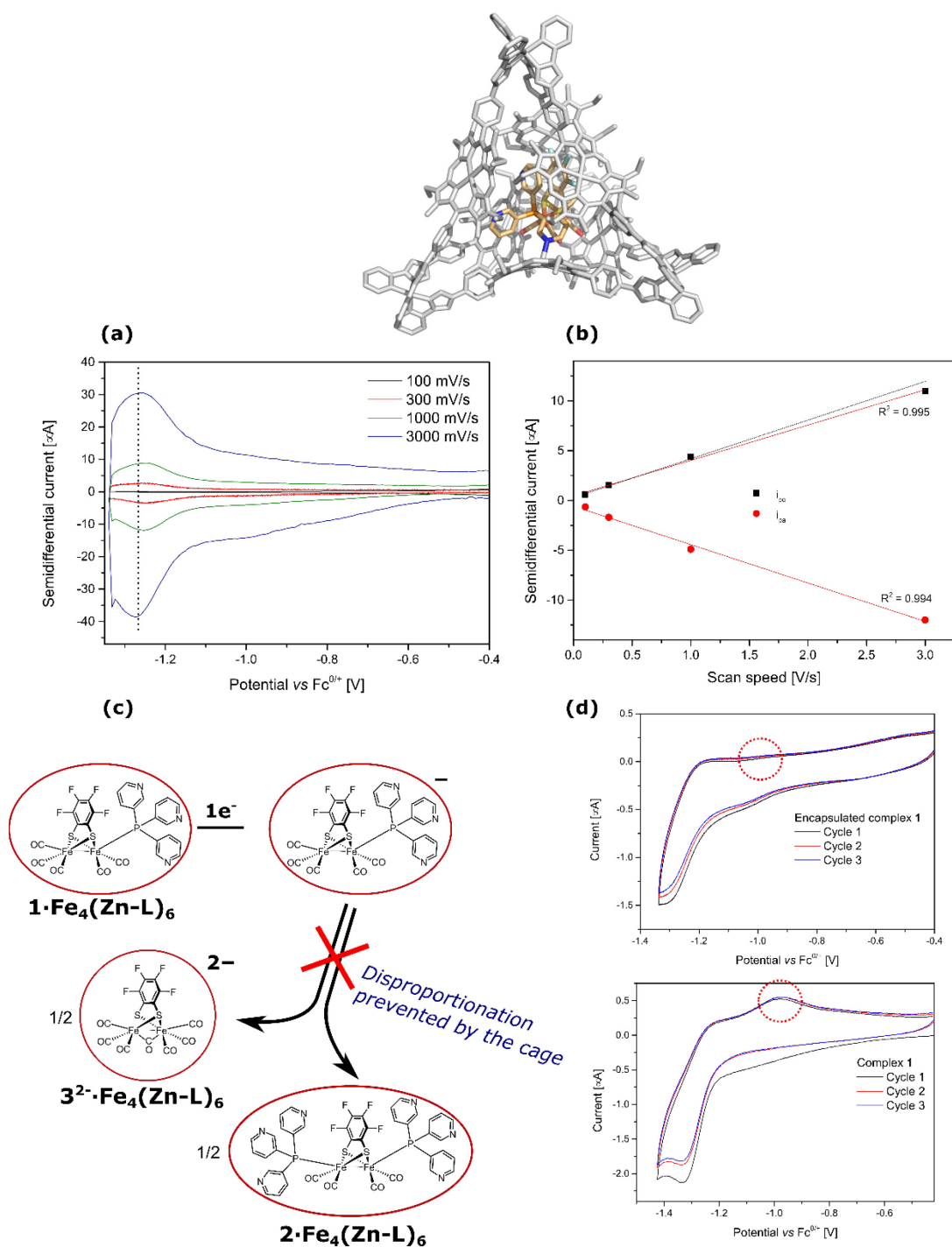


Figure S 28. Redox chemistry of $1 \cdot \text{Fe}_4(\text{Zn-L})_6$ in the absence of acid. (a) Scan rate dependent semidifferential convolution voltammograms of 0.1 mM $1 \cdot \text{Fe}_4(\text{Zn-L})_6$ in acetonitrile containing 0.1 M $n\text{Bu}_4\text{NPF}_6$ as electrolyte. The dotted line shows the overlap between the reduction and re-oxidation waves, indicating that the redox reaction is reversible at each scan speed. (b) Plot of the semidifferential peak current of the reduction wave of **1** against the scan speed indicating that the redox event is solution-based and nearly reversible. The black dotted line would be observed for a fully reversible reduction wave. (c) Disproportionation of **1** upon reduction is prevented by the surrounding cage structure. (d) Repeated cyclic voltammograms at 0.1 V/s of 0.1 mM $1 \cdot \text{Fe}_4(\text{Zn-L})_6$ (top) and 0.1 mM **1** (bottom) indicating that disproportionation is not observed for **1** when it is encapsulated inside the cage. Free **1** shows a redox wave at -1.0 V (vs. Fc/Fc^+) which corresponds to the oxidation of 3^{2-} to **3**. This wave is absent for the encapsulated catalyst, confirming that disproportionation is prevented by the surrounding cage structure.

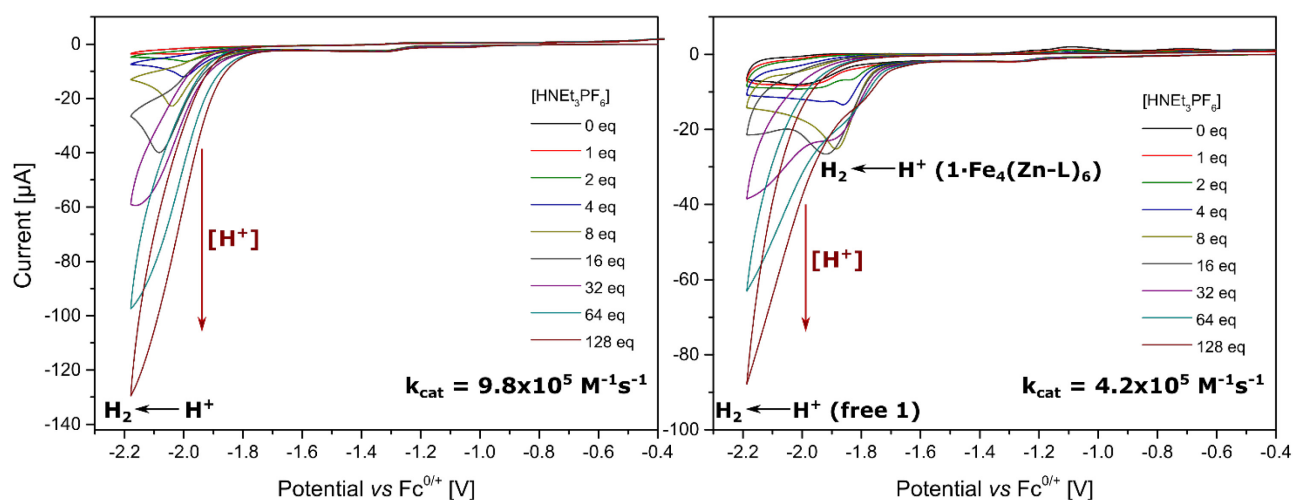
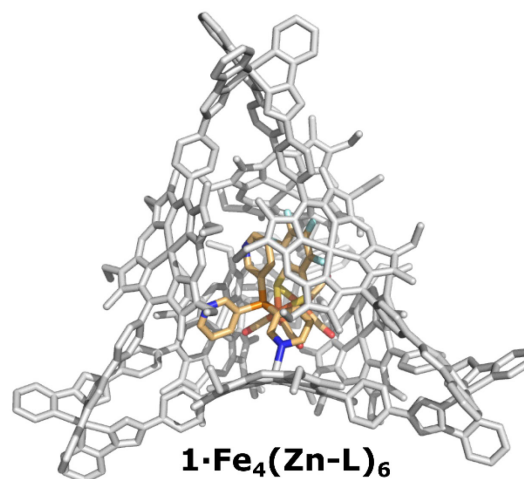
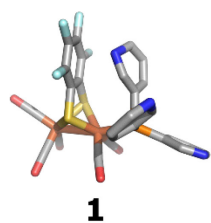


Figure S 29. Electrocatalytic proton reduction in acetonitrile. (left) Cyclic voltammetry of 0.1 mM **1** in acetonitrile containing 0.1 M $n\text{Bu}_4\text{NPF}_6$ and increasing concentrations of the acid HNEt_3PF_6 on a glassy carbon working electrode. (right) Cyclic voltammetry of 0.1 mM **1·Fe₄(Zn-L)₆** in acetonitrile containing 0.1 M $n\text{Bu}_4\text{NPF}_6$ and increasing concentrations of the acid HNEt_3PF_6 on a glassy carbon working electrode. The catalytic wave shifts to a more negative potential after 16 equiv. of acid.

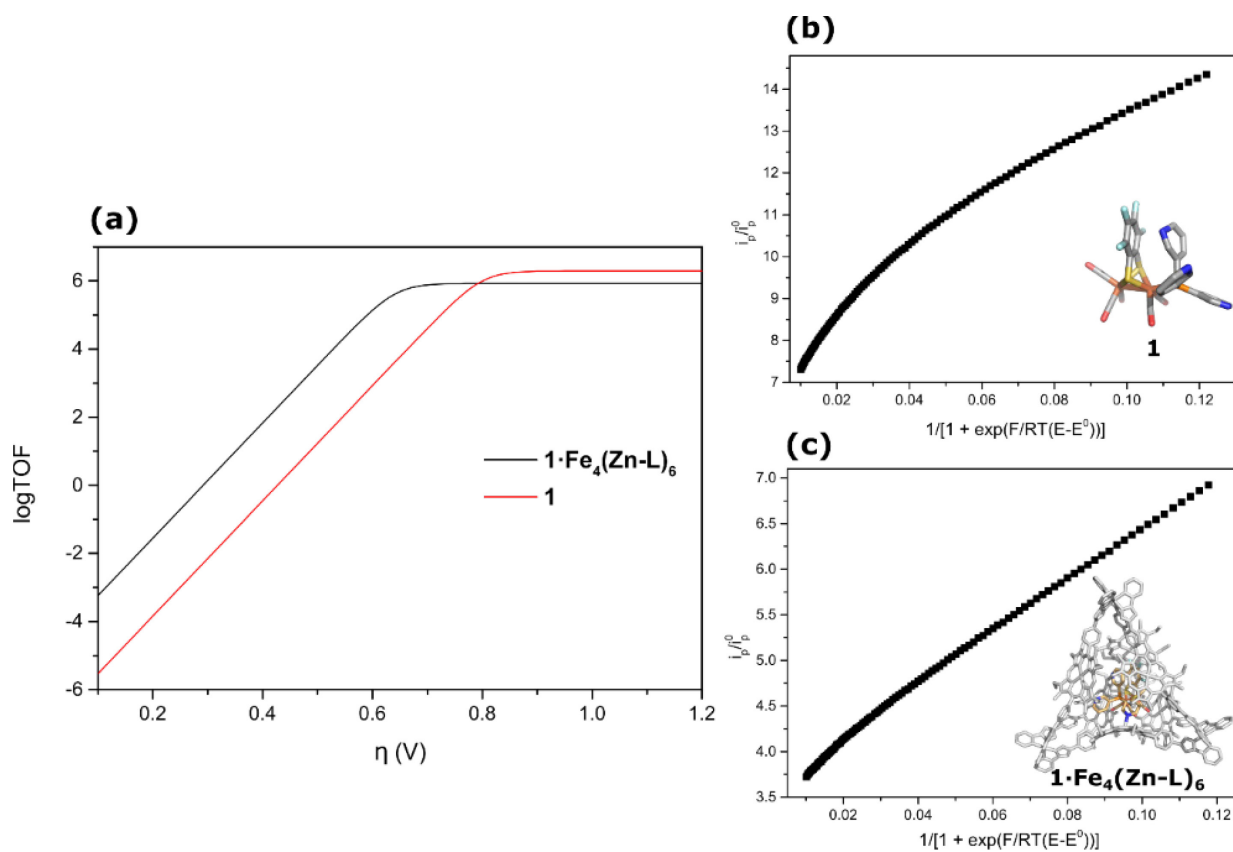


Figure S 30. (a) Tafel plots for **1** and $1 \cdot \text{Fe}_4(\text{Zn-L})_6$ in the presence of the weak acid HNET_3PF_6 in acetonitrile. The value of TOF_{max} is extrapolated for a 1M concentration of protons. (b) Foot-of-the-wave curves for **1** in the presence of the weak acid HNET_3PF_6 in acetonitrile. (c) Foot-of-the-wave curves for $1 \cdot \text{Fe}_4(\text{Zn-L})_6$ in the presence of the weak acid HNET_3PF_6 in acetonitrile. FotW analysis is shown for a single acid concentration for clarity, but the analysis has been averaged over several acid concentrations for **1** and $1 \cdot \text{Fe}_4(\text{Zn-L})_6$.

Spectroelectrochemistry of $1 \cdot \text{Fe}_4(\text{Zn-L})_6$ was attempted. However, it turned out to be challenging as the cage precipitates due to the high electrolyte concentration required in these types of experiments.



Figure S 31. (left) Solution of $1.0 \text{ mM Fe}_4(\text{Zn-L})_6$ in acetonitrile at 298 K. (right) Suspension of $1.0 \text{ mM Fe}_4(\text{Zn-L})_6$ in acetonitrile containing $0.2 \text{ M } n\text{BuNPF}_6$ at 298 K. The high electrolyte concentration leads to cage precipitation, preventing spectroelectrochemical measurements from being performed.

9. ^1H NMR study of **1** in the presence of HNEt_3PF_6

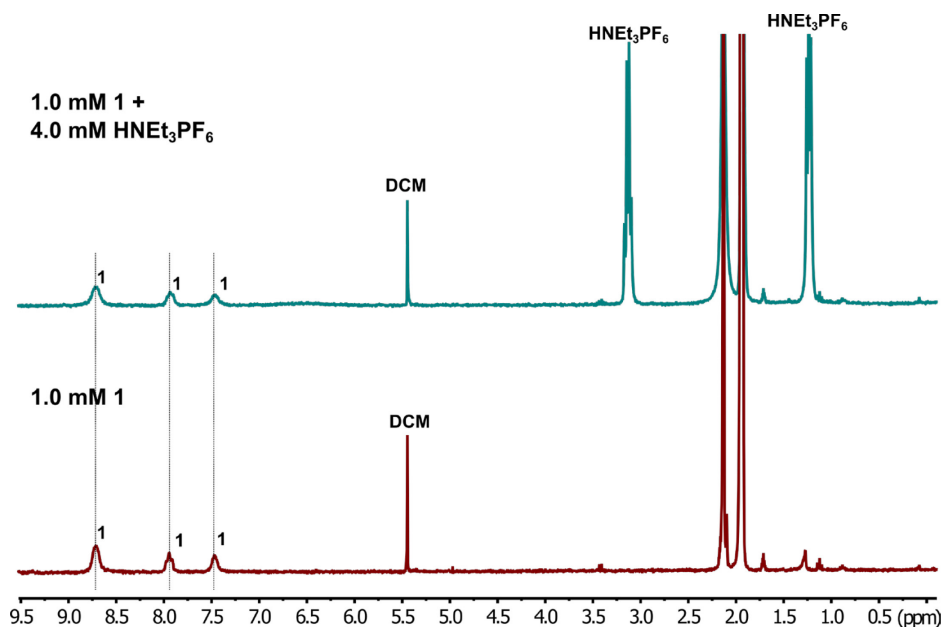


Figure S 32. (top) 1.0 mM **1** in the presence of 4 eq. HNEt_3PF_6 in CD_3CN (298 K, 300 MHz). (bottom) 1.0 mM **1** CD_3CN (298 K, 300 MHz). No shifts are seen for the signals of the catalyst upon addition of acid, confirming that the catalyst is not protonated by the acid.

10. UV-vis study of $\mathbf{1}\cdot\text{Fe}_4(\text{Zn-L})_6$ in the presence of HNEt_3PF_6

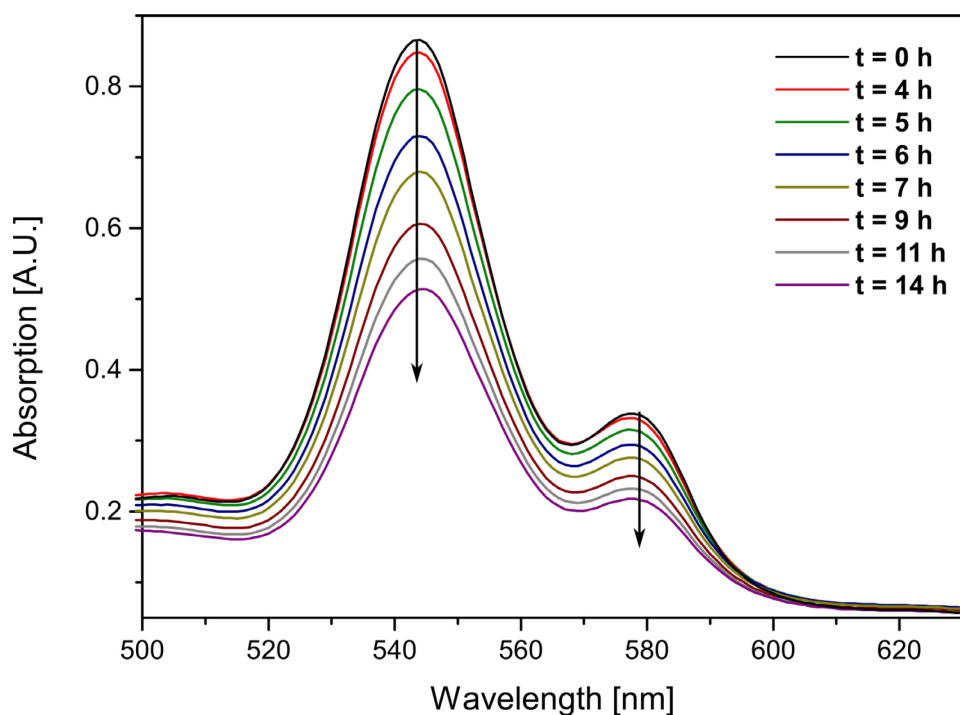


Figure S 33. UV-vis spectrum of $\text{Fe}_4(\text{Zn-L})_6$ (45 μM) in the presence of 64 eq HNEt_3PF_6 in CH_3CN overnight at 298 K, showing slow decomposition of the cage by the decrease in the absorption of the cage porphyrins. Demetallation of the cage does not take place as evident from the Q bands not changing shape in time.

11. References

- 1 R. Zaffaroni, W. I. Dzik, R. J. Detz, J. I. van der Vlugt and J. N. H. Reek, *Submitt. to Eur. J. Inorg. Chem.*
- 2 S. Saba, R. Hernandez, C. C. Choy, K. Carta, Y. Bennett, S. Bondi, S. Kolaj and C. Bennett, *J. Fluor. Chem.*, 2013, **153**, 168–171.
- 3 X. Wang, S. S. Nurttala, W. I. Dzik, R. Becker, J. Rodgers and J. N. H. Reek, *Chem. Eur. J.*, 2017, **23**, 14769–14777.
- 4 S. S. Nurttala, W. Brenner, J. Mosquera, K. M. Van Vliet, J. R. Nitschke and J. N. H. Reek, *Chem. Eur. J.*
- 5 W. Brenner, T. K. Ronson and J. R. Nitschke, *J. Am. Chem. Soc.*, 2017, **139**, 75–78.
- 6 S. Grimme, C. Bannwarth and P. Shushkov, *J. Chem. Theory Comput.*, 2017, **13**, 1989–2009.
- 7 J. Cremers, S. Richert, D. V. Kondratuk, T. D. W. Claridge, C. R. Timmel and H. L. Anderson, *Chem. Sci.*, 2016, **7**, 6961–6968.
- 8 P. Bhyrappa, V. Krishnan and M. Nethaji, *J. Chem. Soc. Dalt. Trans.*, 1993, 1901–1906.
- 9 L. Favereau, A. Cnossen, J. B. Kelber, J. Q. Gong, R. M. Oetterli, J. Cremers, L. M. Herz and H. L. Anderson, *J. Am. Chem. Soc.*, 2015, **137**, 14256–14259.
- 10 M. J. D. Powell, in *Advances in Optimization and Numerical Analysis*, Springer Netherlands, Dordrecht, 1994, pp. 51–67.
- 11 D. Bray and S. Lay, *Comput. Appl. Biosci.*, 1994, **10**, 471–6.
- 12 D. Brynn Hibbert and P. Thordarson, *Chem. Commun.*, 2016, **52**, 12792–12805.